

AWARD NUMBER:

W81XWH-06-2-0067

PROJECT TITLE:

Alliance for NanoHealth Competitive Research Program

PRINCIPAL INVESTIGATOR:

Jodie L. Conyers, PhD

CONTRACTING ORGANIZATION:

The University of Texas Health Science Center at Houston
Houston, Texas 77030

REPORT DATE:

October 2009

TYPE OF REPORT:

Annual

PREPARED FOR:

U.S. Army Medical Research and Materiel Command
Fort Detrick, Maryland 21702-5012

DISTRIBUTION STATEMENT:

Approved for Public Release;
Distribution Unlimited

The views, opinions and/or findings contained in this report are those of the author(s) and should not be construed as an official Department of the Army position, policy or decision unless so designated by other documentation.

REPORT DOCUMENTATION PAGE			<i>Form Approved</i> <i>OMB No. 074-0188</i>	
Public reporting burden for this collection of information is estimated to average 1 hour per response, including the time for reviewing instructions, searching existing data sources, gathering and maintaining the data needed, and completing and reviewing this collection of information. Send comments regarding this burden estimate or any other aspect of this collection of information, including suggestions for reducing this burden to Washington Headquarters Services, Directorate for Information Operations and Reports, 1215 Jefferson Davis Highway, Suite 1204, Arlington, VA 22202-4302, and to the Office of Management and Budget, Paperwork Reduction Project (0704-0188), Washington, DC 20503				
1. Agency Use Only (Leave blank)		2. Report Date 28-OCT-2009		3. Report Type and Period Covered Annual 29 SEP 2008 - 28 SEP 2009
4. Title and Subtitle Alliance for NanoHealth Competitive Research Program			5. Award Number W81XWH-06-2-0067	
6. Author(s) Jodie L. Conyers, PhD ; Email: Jodie.L.Conyers@uth.tmc.edu				
7. Performing Organization Name The University of Texas Health Science Center at Houston 6410 Fannin Houston, Texas 77030 email: Jodie.L.Conyers@uth.tmc.edu			8. Performing Organization Report Number (Leave Blank)	
9. Sponsoring/Monitoring Agency Name and Address U.S. Army Medical Research and Materiel Command Fort Detrick, Maryland 21702-5012			10. Sponsoring/Monitoring Agency Report Number (Leave Blank)	
11. Supplementary Notes (i.e., report contains color photos, report contains appendix in non-print form, etc.) report contains color photos and tables, report contains appendix				
12a. Distribution/Availability Statement (check one) <input checked="" type="checkbox"/> Approved for public release; distribution unlimited				12b. Distribution Code (leave blank)
13. Abstract (<i>Maximum 200 Words</i>) Through the work performed within the T5 program, Houston will become well prepared for the adverse effects of terrorism and natural disasters. The University of Texas Health Science Center at Houston has organized a highly qualified team within the Texas Medical Center for addressing the plurality of concerns that arise during public health crises. The ultimate goal of the T5 program will be to solve a wide variety of public health, scientific, and medical issues that will eventually lead to enhanced community preparedness. As part of the T5 program, training and education as well as predictive strategies will be explored to enhance disaster response. Diagnostic and therapeutic measures will be developed to assess and treat injury and disease. Fundamental scientific research will also be performed in order to better understand the physiological response to injury and disease. No other comprehensive program matches the combined technology, medical expertise, fundamental science, and training that encompass the T5 program. Under the direction of Dr. S. Ward Casscells and other leaders of the Texas Medical Center, the T5 program will provide the blueprint that other cities will use to better prepare their communities for public health disasters.				
14. Subject Terms (keywords previously assigned to proposal abstract or terms which apply to this award)				15. Number of Pages 43
				16. Price Code
17. Security Classification of Report Unclassified	18. Security Classification of this Page Unclassified	19. Security Classification of Abstract Unclassified		20. Limitation of Abstract Unlimited

TABLE OF CONTENTS

2. Program Overview	5
3. Project 1.....	6
<i>On-Command Control of Blood Poll Residence Time for Nanoparticle-based Molecular Imaging</i>	
4. Project 2.....	7
<i>Nanomagnetic Biosensors for Cancer Diagnostics</i>	
5. Project 3.....	8
<i>Modulation of Inner Ear Nanomechanics</i>	
6. Project 4.....	9
<i>Development of Asymmetric Liposome Nanoparticles for Targeted Delivery of siRNA to Silence Cyclin D1 Expression and Tumor Regression in Hepatocellular Carcinoma</i>	
7. Project 5.....	10-14
<i>Nanorods-Mediated Gene Therapy in Bladder Cancer</i>	
8. Project 6.....	15-24
<i>Magnetic Drug-Loaded Nanoparticles for Targeted Therapy</i>	

9. Project 7.....	25-35
<i>Guided Microvasculature Formation and Cellular Infiltration for Tissue Regeneration Applications in Nano-Structured Silk-Fibroin-Chitosan Scaffolds</i>	
10. Project 8.....	36
<i>Development of Nanotherapeutics to Enhance Wound Healing</i>	
11. Project 9.....	37
<i>Self-Asembling Peptide-Amphiphile Nanofiber Networks for the Controlled Growth and Differentiation of Dental Stem Cells</i>	
12. Project 10.....	38-43
<i>Feasibility of Selective Laser Elimination of Leukemia Cells Targeted with Gold and Silver Nanorods</i>	

PROGRAM OVERVIEW

The Alliance for NanoHealth Competitive Research Program reviewed more than 70 proposals in the summer of 2006 and awarded ten seed grants for new collaborative projects that combined nanotechnology and medicine. After three years, all projects have come to an end and at least half have received follow-on funding from the NIH, DoD, or private foundations.

Included in this report are research activities reported for four of the five projects that carried funding into the last performance period spanning September 2008 through September 2009. The only project that charged research expenditures to the program during the most recent performance period was Project 8, led by Dr. Joan Nichols of the University of Texas Medical Branch.

Now that all invoicing has been closed out, approximately \$150,000 is remaining and will be allocated a new seed project that combined nanotechnology and medicine. This new project has been discussed with the program COR and we will soon submit a Scope of Work and Detailed Budget to TATRC in order to carry forward these funds for an additional year. This project will focus on the development of a microfluidics nanosensor platform that can rapidly screen biomarkers associated with multiple organ failure (MOF). This technology is highly relevant to ICU patients recovering from severe trauma and provides clinicians with rapid on-site diagnostics and provide improved care to those patients most susceptible to MOF.

PROJECT 1

On-Command Control of Blood Pool Residence Time for Nanoparticle-Based Molecular Imaging

Vikas Kundra, MD, PhD (M.D. Anderson Cancer Center)

Ananth Annapragade, PhD (University of Texas Health Science Center at Houston)

This project was completed at the end of the second performance period (September 2007 – September 2008) and did not report any spending beyond October 2008. Therefore, no annual report required for this project in the current performance period.

PROJECT 2

Nanomagnetic Biosensors for Cancer Diagnostics

Dmitri Litvinov, PhD (University of Houston)
Mini Kapoor, PhD (M.D. Anderson Cancer Center)

This project was completed at the end of the first performance period (June 2006 – September 2007) and did not report any spending beyond October 2007. Therefore, no annual report required for this project in the current performance period.

PROJECT 3

Modulation of Inner Ear Nanomechanics

John Oghalai, MD (Baylor College of Medicine)
Bahman Anvari, PhD (Rice University)

This project was completed at the end of the second performance period (September 2007 – September 2008) and did not report any spending beyond October 2008. Therefore, no annual report required for this project in the current performance period.

PROJECT 4

Developmet of Asymmetric Liposome Nanoparticles for Targeted Delivery of siRNA to Slience Cyclin D1 Expression and Tumor Regression in Hepatocellular Carcinoma

Sundararajah Thevananther, PhD (Baylor College of Medicine)
Kishore Mohanty, PhD (University of Houston)

This project was completed at the end of the second performance period (September 2007 – September 2008) and did not report any spending beyond October 2008. Therefore, no annual report required for this project in the current performance period.

PROJECT 5

Nanorods-Mediated Gene Therapy in Bladder Cancer

Liana Adam, PhD (M.D. Anderson Cancer Center)

Jason Hafner, PhD (Rice University)

Introduction

The overall goal of this project is to non-covalently complex genetic material to gold nanorods, deliver the nanorods into specific cells by receptor mediated endocytosis, and then release the genetic material by locally heating the gold nanorods with radiation at their plasmon resonant absorption in the near infrared. The subcontract project to Hafner's lab at Rice focuses on the synthesis and optical properties of the nanorods, and the interfacial chemistry required to functionalize the nanorods with monoclonal antibodies.

The nanorods are formed by the growth of colloidal gold seeds in the presence of the surfactant cetyltrimethylammonium bromide (CTAB). Gold nanorods are of particular interest for biomedical applications due to their small size and potentially improved permeation into tissue relative to larger tunable gold nanoparticles. However, gold nanorods and other shapes synthesized with CTAB are also stabilized by this strong surfactant, which is thought to form a bilayer on the nanoparticle surface.¹ If the CTAB is removed from solution, the nanorods immediately aggregate.²

This report describes progress on two aspects of biological targeting of CTAB-synthesized gold nanorods that occurred during the reporting period. First, the sensitivity of nanorod stability to CTAB concentration has been carefully characterized. Second, a simple chemical strategy has been developed to create nanorod-antibody conjugates based on strong gold-thiol and amide bonds that specifically target cells.

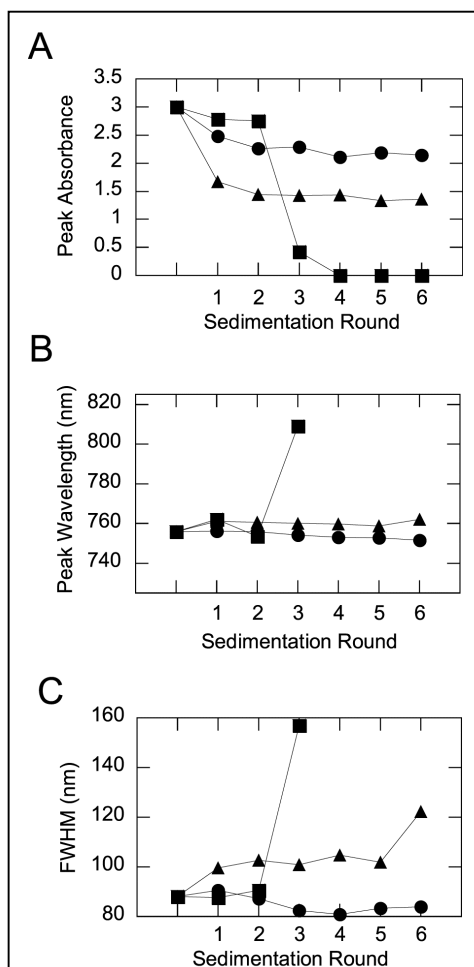


Figure 1. The evolution of the plasmon resonant peak of nanorod solutions after reduction of the CTAB concentration by sedimentation. The absorbance peak height (A), peak wavelength (B), and peak width (C) for CTAB stabilized gold nanorods (■), anionic polymer stabilized gold nanorods (▲), and PEGylated nanorods (●).

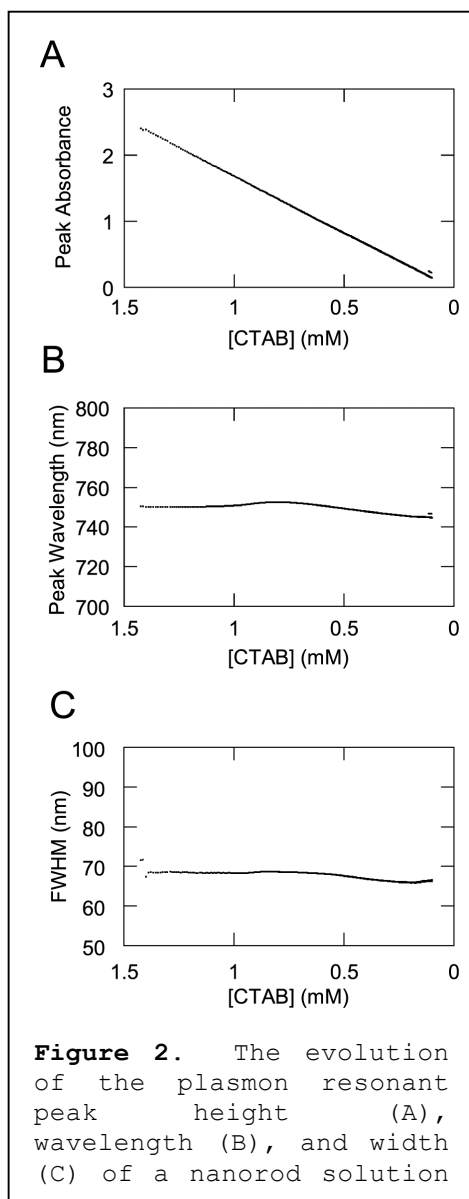
Results & Discussion

Nanorod Stability

In order to determine the critical CTAB concentration required for nanorod stability, and to understand the nature of the stabilization, the CTAB concentration was lowered in three ways. First, aliquots of nanorods were pelleted by sedimentation, 90% of the clear supernatant was removed, and the nanorod pellets were resuspended to their initial volume with water. In this way the CTAB concentration was reduced by a factor of 10 on each round of sedimentation. The LSPR peak wavelength, width, and height were recorded after each round of sedimentation and are plotted in Figure 1 (squares). There was essentially no nanorod aggregation, *i.e.* no LSPR peak height reduction, broadening, or red shift, until the third round of sedimentation. Therefore, nanorod aggregation occurred somewhere between 1 and 0.1 mM CTAB.

Second, the CTAB concentration of a nanorod solution was monitored during slow dilution with water (Figure 2). As expected, the LSPR peak absorbance decreased as the nanorod concentration was reduced. However, the LSPR peak wavelength and width were not affected, indicating no aggregation, although the CTAB concentration was reduced to below 50 mM. This apparent inconsistency with the results of Figure 1 reveals that it is the ratio of CTAB concentration to nanorod concentration that determines stability, not the CTAB concentration alone, which is typical for surfactant-stabilized colloids.

Third, CTAB was removed from a nanorod solution without reducing the nanorod concentration by extraction with chloroform. Based on our own measurement of the distribution ratio for CTAB between water and chloroform, the aggregation occurred between 370 mM and 290 mM CTAB. Given that the nanorod concentration was 0.5 nM, the critical CTAB/nanorod concentration ratio was approximately 740,000. Note that this number of CTAB molecules per nanorod is much larger than the amount of CTAB needed to simply coat the nanorods with a surfactant bilayer, so the dynamic interactions between CTAB in solution and in the bilayer must be important for nanorod stability.

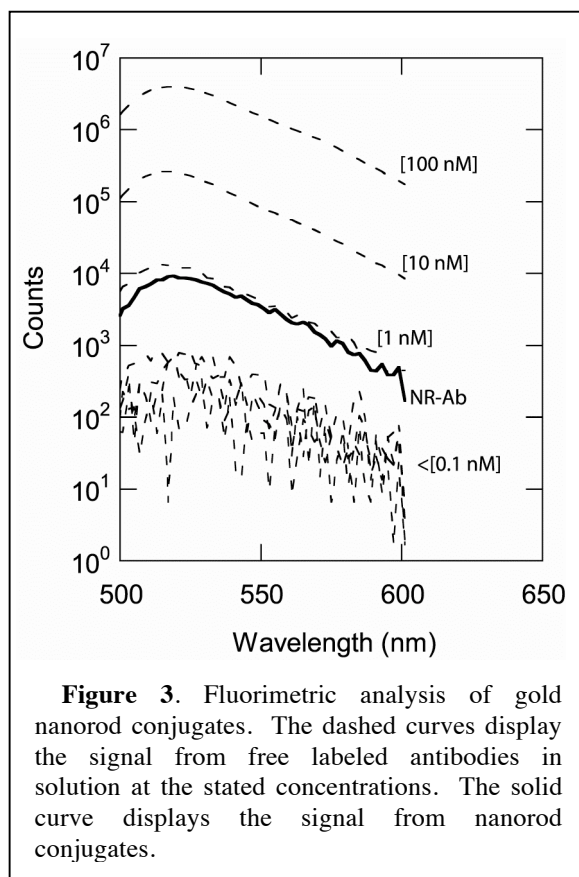


The above results demonstrate that CTAB must be maintained at a concentration on the order of 0.1 mM, which is too high for use in cell culture due to the inherent cytotoxicity of the surfactant. Therefore, two methods of nanorod stabilization were compared. Nanorods were stabilized by displacement of the CTAB with a thiol-terminal polyethylene glycol (mPEG-SH), and by wrapping the CTAB bilayer with polystyrene sulfonate (PSS). The LSPR peak wavelength, width, and height after successive rounds of sedimentation are displayed in Figure 1. While the unstabilized nanorods aggregated after the third round of sedimentation, both PEGylation and polyelectrolyte stabilization were effective. However, PEGylation maintained a narrower LSPR peak, indicating a reduced degree of aggregation relative to polyelectrolyte stabilization.

Nanorod Bioconjugation

To form stable nanorod bioconjugates, a heterobifunctional polyethylene glycol with thiol and carboxyl end groups (HOOC-PEG-SH) was applied. Nanorod stabilization with HOOC-PEG-SH yielded identical results to mPEG-SH in Figure 1. The carboxy-terminal nanorods were conjugated to antibodies using the zero-length crosslinker EDC stabilized by NHS.³ Standard procedures for EDC protein crosslinking were followed,⁴ with the following modifications for the unique properties of the carboxy-terminal nanorods. First, since the functionalized nanorod surfaces contain no amines, there is no chance of nanorod aggregation due to amide bond formation between nanorods, which minimizes the criticality of the initial EDC exposure. Second, to avoid the need for buffer exchange or sedimentation, the change in pH from 6.1 for activation to 7.1 for conjugation was accomplished by diluting the nanorods into a larger volume of antibody solution. Finally, sedimentation was performed (rather than buffer exchange) to remove excess reactants and products from the nanorod solution.

To characterize the final product, nanorods were conjugated to AF-Ab for fluorimetric analysis. After the steps described above, the nanorod conjugates were put through successive rounds of sedimentation, 90% decantation, and resuspension in buffer to dilute the unbound AF-Ab by factors of ten. Fluorimetry

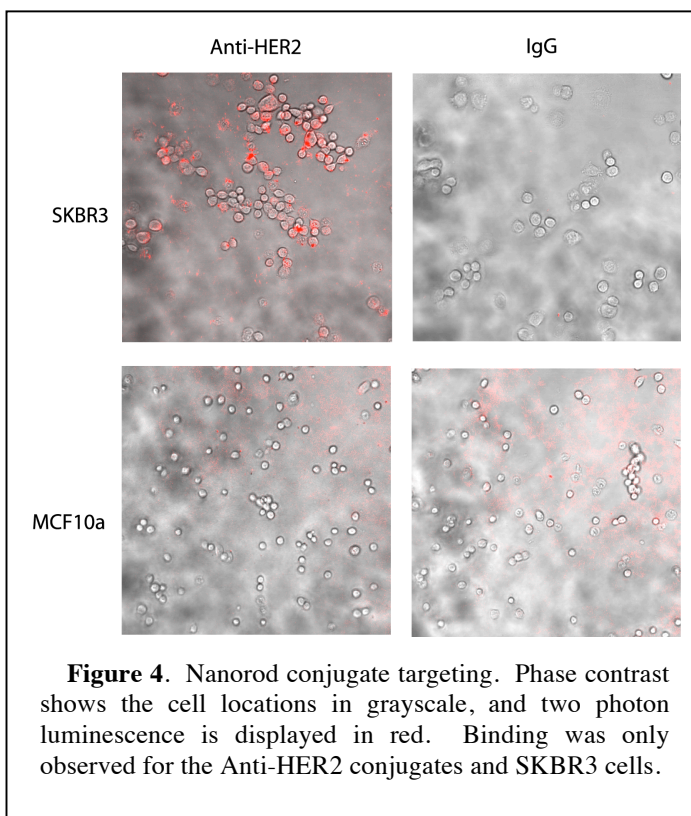


of unbound AF-Ab in the decants, shown in Figure 3, serves as a standard curve and reaches the background fluorescence noise floor by the 4th round at an AF-Ab concentration of 0.1 nM. Fluorimetry of the nanorod conjugates solution indicated a nanorod bound AF-Ab concentration of 1 nM, which yields approximately two antibodies per nanorod given a nanorod concentration of 0.5 nM based on the LSPR extinction peak.²

Nanorod conjugate targeting was tested with an in vitro system. Nanorods were conjugated to anti-HER2 and also to rabbit IgG as a control. Each conjugate was incubated with both the HER2-overexpressing epithelial breast cancer cell line SK-BR-3 and the normal mammary epithelial cell line MCF10A for 30 minutes simultaneously and under identical conditions. The cells were washed and immediately imaged live by two photon luminescence, which highlights the presence of gold particles,⁵ as well as phase contrast to show the cell locations. Figure 4 demonstrates that only the specific antibody/cell produced a significant level of nanorod binding to the cells.

Key Research Accomplishments

To maintain colloidal stability, it is the ratio of CTAB to nanorod concentration that must be maintained. Here, the critical CTAB:nanorod ratio was found to be approximately 740,000:1. The CTAB layer can be displaced by thiol terminal PEG, or wrapped by polyelectrolytes. However, gold-thiol PEGylation results in higher yields and more monodisperse nanorod samples when the CTAB is removed. A bifunctional PEG with thiol and carboxyl end groups results in carboxy-terminal PEGylated nanorods which can be conjugated to antibodies via a carbodiimide linking agent. A fluorimetry assay reveals approximately two antibodies per nanorod. The nanorod conjugates demonstrated specific targeting in two different antibody/cell systems as observed by two-photon luminescence.



Conclusions

Methods were developed to stabilize isolate gold nanorods from their cytotoxic stabilizing surfactant and conjugate monoclonal antibodies to their surface. The resulting nanorod bioconjugates specifically bind the targeted cells, and can be used for specific delivery of genetic material.

Presentations

“Synthesis, Optics, and Biological Applications of Plasmon Resonant Gold Nanoparticles”, 2nd Symposium of the Asian Research Network, Seoul, South Korea, May 17, 2009.

“Biological Sensing and Interaction Analysis with Localized Surface Plasmon Resonance”, Emerging Technologies for Systems Biology Symposium, M.D. Anderson Cancer Center, Houston, TX August 12, 2009.

Publications

B. C. Rostro-Kohanloo, L. R. Bickford, C. M. Payne, E. S. Day, L. J. E. Anderson, M. Zhong, S. Lee, K. M. Mayer, T. Zal, L. Adam, C. P. N. Dinney, R. A. Drezek, J. L. West, and J. H. Hafner, “The stabilization and targeting of surfactant-synthesized gold nanorods”, *Nanotechnology* **20**, p434005, 2009.

References

1. Nikoobakht, B.; El-Sayed, M. A., Evidence for bilayer assembly of cationic surfactants on the surface of gold nanorods. *Langmuir* **2001**, 17, (20), 6368-6374.
2. Liao, H.; Hafner, J., Gold nanorod bioconjugates. *Chemistry of Materials* **2005**, 17, (18), 4636-4641.
3. Grabarek, Z.; Gergely, J., Zero-Length Crosslinking Procedure with the Use of Active Esters. *Analytical Biochemistry* **1990**, 185, (1), 131-135.
4. Hermanson, G. T., *Bioconjugate Techniques*. 1st ed.; Academic Press: 1996; p 785.
5. Wang, H.; Huff, T. B.; Zweifel, D. A.; He, W.; Low, P. S.; Wei, A.; Cheng, J.-X., In vitro and in vivo two-photon luminescence imaging of single gold nanorods. *Proceedings of the National Academy of Sciences of the United States of America* **2005**, 102, (44), 15752-15756.

PROJECT 6

Magnetic Drug-Loaded Nanoparticles for Targeted Therapy

Jim Klostergaard, PhD (M.D. Anderson Cancer Center)

Joan Bull, MD (University of Texas Health Science Center at Houston)

David Gorenstein, PhD (University of Texas Health Science Center at Houston)

Introduction

Breast cancer is the most common cancer in women in the U.S. Although combination chemotherapy improves survival in some metastatic breast cancer patients, this disease is generally currently incurable and new treatment approaches are needed. A subtype of breast cancer, inflammatory breast cancer (IBC), currently has no novel therapeutic options and has high rates of recurrence after conventional treatment. Both drug-resistance and inadequate drug delivery to the tumor have been proposed to contribute to this dilemma. The use of magnetically-vectorable, drug-loaded nanoparticles (NP) is proposed to be capable of achieving superior tumor pharmacokinetics compared to that of free drugs as currently practiced. The initial clinical presentation of IBC is superficial, in the skin, and the skin is known to harbor residual disease as it is the primary site of loco-regional recurrence after maximal therapy. The proposed approach using magnetic vectoring of magnetically-responsive NPs (MNPs) would exploit this superficial presentation, accessible to the required magnetic field strengths and gradients inherent in currently available permanent magnets: thus, being translatable to clinical application if validated pre-clinically.

Macromolecular drug delivery systems have been developed as one approach to overcome drug resistance and improve drug therapeutic index. Such polymeric drug conjugates are internalized by endocytosis, resulting in lysosomal accumulation and release of drug from polymer (activation). Drug copolymers may have key advantages over free drugs, including reduced toxicity. High plasma C_{max} values and rapid extravasation, which contribute to the toxicity of free drugs, should be largely abrogated with copolymer prodrugs, whose size limits diffusion rates. However, the enhanced permeability and retention (EPR) effect should still allow copolymer accumulation and retention within the tumor interstitium, followed by prodrug activation. These pharmacological principles also generally apply to NP drug carriers, whether serving as components of prodrugs or simply requiring degradation at the tumor.

NPs hold several potential advantages over other carriers for drug delivery to tumors. Drugs with diverse physical-chemical properties can be incorporated, depending on the matrix or linker chemistry selected. In addition, NPs tend to have markedly higher drug loading capacities than other delivery systems. The drug payload can be embedded in matrices whose physical-chemical properties dictate the characteristics of drug release. Finally, NP surfaces can be easily

modified with targeting ligands, such as the anti-CD44 thioaptamers we propose herein.

The concept of using MNPs for driving a desired physiological event, such as drug delivery, originated in the late 70's, but has heretofore faced significant technical issues that have hindered advancement of this technology. First, macroparticles attract each other in a magnetic field, causing aggregation, an undesirable outcome. Second, achieving both sufficient therapeutic drug loading levels and chemical functionality have proven to be difficult technical hurdles to overcome. Finally, the technology for effective control of the MNPs in a physiological environment has not been available. However, recent significant technological advancements have occurred to bring targeted magnetic therapies within the realm of functional potential, including: 1) dense, spherical, single domain magnetite MNPs can now be produced uniformly and economically, 2) novel methods now exist for attachment of functional groups to NPs, and 3) new electromagnetic instrumentation is available for vectored NP navigation and positioning.

The application of nanotechnology, and NPs in particular, to breast cancer is only in its infancy. One relevant development is the recently FDA-approved Abraxane™, a Cremophor-free, albumin-NP-bound paclitaxel formulation, for second-line breast cancer treatment. It achieved superior response rates compared to the 175 mg/m² Taxol arm in its registration trial; however, comparisons to Taxotere remain to be conducted, and other indications have not yet been explored.

The CD44 proteoglycan family, including the standard (S) form and 10 or more known splice variants, is expressed on most human breast cancer cell lines. Among a panel of 110 breast carcinomas, 60% were positive for CD44s, 79% for v5, 74% for v6, 54% for v7 and 95% for v3-10. Its wide expression makes it an attractive candidate for targeting breast cancer, including IBC.

Thus, we introduced the concept of bimodal vectoring: an initial phase driven by the magnetic field influence on MNP localization to the tumor; and a secondary, diffusion-controlled, post-magnetic vectoring phase, driven by a binding moiety (anti-CD44 thioaptamer) that will bind to cell-surface CD44 and precipitate an internalization event.

Results & Discussion

Synthesis of CD44 HABD (Hyaluronan Binding Domain) protein by cell free expression.

Due to the poor yields of protein using a bacterial *in vivo* expression system, we used a cell-free expression system to produce the CD44 HABD domain (residues 20-172). Cell-free expression methods offer tremendous advantages over the traditional, *in vivo* expression systems. The main advantages of cell-free expression methods include rapid, often one-step purification of the protein of interest, small working volumes (μL of volumes compared to mL-L of volumes of

bacterial cell cultures), and elimination of laborious procedures of cloning and cell culture.

Combinatorial Selection of Monothio DNA aptamers targeting CD44 HABD

The initial library was constructed by PCR-amplification of a chemically synthesized, 73-nt DNA template (a 30-nt random region flanked by a 22-nt and a 21-nt PCR primer regions). Before PCR amplification, the single-stranded DNA template was subjected to Klenow reaction to yield a double-stranded DNA template. During the PCR, dATP(α S) was used along with dCTP, dGTP and dTTP, so the resulting DNA library will have monothio-substituted phosphoryl groups at the 5'-end of each dA residue.

5'-GAGATTCATCACGCGCATAGTC-N₃₀-CGACTATGCGATGATGTCTTC-3'

Selection of thioaptamers was performed on the His-tagged CD44 HABD that was bound to the Ni-NTA (Nickel Nitrolo Triacetic Acid) beads (Qiagen). Before the initial round of selection, the thioapatamer library was screened against the bare Ni-NTA beads to eliminate the DNA sequences that would bind to the beads themselves. After 10 rounds of selection, the sequences of the selected thioaptamers showed convergence.

The selected sequences are shown below.

	10	20	30	40	50	60	70
10-7/1-73	CAT	CACGCGCATAGTCTG	TG	TG	TG	TG	TG
10-13/1-73	CAT	CACGCGCATAGTCTT	GG	TG	TG	TG	TG
10-3/1-73	CAT	CACGCGCATAGTCCCA	A	GG	CT	TG	CAAGGG
10-19/1-72	CAT	CACGCGCATAGTCCCA	A	GG	CT	TG	CAAGGG
10-29/1-73	CAT	CACGCGCATAGTCCCA	A	GG	CT	TG	CAAGGG
10-5/1-72	CAT	CACGCGCATAGTCCCA	A	GG	CT	TG	CAAGGG
10-22/1-72	CAT	CACGCGCATAGTCCCA	A	GG	CT	TG	CAAGGG
10-26/1-73	CAT	CACGCGCATAGTCCCA	A	GG	CT	TG	CAAGGG
10-9/1-73	CAT	CACGCGCATAGTCCCA	A	GG	CT	TG	CAAGGG
10-24/1-72	CAT	CACGCGCATAGTCAACAT	GGATC	TG	CAAGGG	T	AACCAAGA
10-27/1-73	CAT	CACGCGCATAGTCCCA	A	GATAC	TG	CAAGGG	T
10-8/1-74	CAT	CACGCGCATAGTCTGCA	A	GG	CT	TG	CAAGGG
10-20/1-72	CAT	CACGCGCATAGTCTGCA	A	GG	CT	TG	CAAGGG
10-4/1-72	CAT	CACGCGCATAGTCCGTA	A	GG	CT	TG	CAAGGG
10-28/1-71	CAT	CACGCGCATAGTCTGCA	A	GG	CT	TG	CAAGGG
10-6/1-73	CAT	CACGCGCATAGTCTGTT	A	GG	CT	TG	CAAGGG
10-30/1-73	CAT	CACGCGCATAGTCTGAAT	A	GG	CT	TG	CAAGGG
10-1/1-73	CAT	CACGCGCATAGTCTCGTT	A	GG	CT	TG	CAAGGG
10-10/1-70	CAT	CACGCGCATAGTCTGTT	A	GG	CT	TG	CAAGGG
10-23/1-73	CAT	CACGCGCATAGTCTGTT	A	GG	CT	TG	CAAGGG
10-2/1-72	CAT	CACGCGCATAGTCCGCGC	A	GG	CT	TG	CAAGGG
10-12/1-72	CAT	CACGCGCATAGTCCGCGC	A	GG	CT	TG	CAAGGG
10-16/1-73	CAT	CACGCGCATAGTCCGCGC	A	GG	CT	TG	CAAGGG
10-14/1-73	CAT	CACGCGCATAGTCTCCAC	A	GG	CT	TG	CAAGGG
10-11/1-73	CAT	CACGCGCATAGTCTTGG	A	GG	CT	TG	CAAGGG
10-17/1-73	CAT	CACGCGCATAGTCTTGG	A	GG	CT	TG	CAAGGG
10-18/1-73	CAT	CACGCGCATAGTCTTGG	A	GG	CT	TG	CAAGGG
10-21/1-73	CAT	CACGCGCATAGTCTTGG	A	GG	CT	TG	CAAGGG

Primers

Primers

Based on the random region sequences, the selected thioaptamers were grouped into six groups. The sequence for each group is shown below

1. *Primer-region-CC**AAGGCCTGCAAGGGAACCAAGGACACAGC**-primer-region*
2. *Primer-region-CC**AAGGCATGCAAGGGAACCAAGGACACAGC**-primer-region*
3. *Primer-region-TGC**AGATGCAAGGTAACCATATCCAAAGCA**-primer-region*
4. *Primer-region-CGT**ATGCAAGGTGAAAGCAGCACACCAATAC**-primer-region*
5. *Primer-region-GCGGC**AGTAGTTGATCCCGAAGCGTTACGAC**-primer-region*
6. *Primer-region-TTGGG**ACGGTGTTAAACGAAAGGGGACGACC**-primer-region*

The consensus sequence of the selected thioaptamers, after 10 rounds of selections, is shown below.

dGAGATTTCATCACGCGCATAGTCCCAAGGCCTGCAAGGGAACCAAGGACACAGCGACTATGCGATGATGTCTTC

The primer regions are shown in blue and the random region is in black. The binding affinities of these selected thioaptamers will be tested in 96-well ELISA plates and the tightest binding thioaptamer used for the nanoparticle conjugation. We will also identify a dithioate (PS2)-modified variation of the top monothioate-backbone modified (PS) thioaptamer to further enhance the affinity and nuclease resistance of the CD44 targeting thioaptamer. We will utilize our bead-based thioaptamer combinatorial library with FACS selection targeting the CD44 HABD.

Synthesis, Characterization and Biocompatibility of SiMNP and TXL Constructs

SiMNP, magnetite in composition and surface-coated with silica (SiO₂), were synthesized according to a modification of the Massart procedure, which enabled the subsequent formation of discrete silica-coated MNP (20 – 30nm diameter) nanodispersions. Silica coatings were achieved through the stoichiometric addition of sodium silicate to an MNP nanodispersion under controlled conditions of decreasing pH, designed to control shell thickness by silica deposition. The chemical/physical properties were characterized by X-ray diffraction to confirm magnetite composition and crystal structure, by energy dispersive x-ray spectroscopy (EDS) to confirm the presence of silica coatings, by TEM to confirm particle size and size distributions for MNP and SiMNP (10–20nm and 20-30nm)

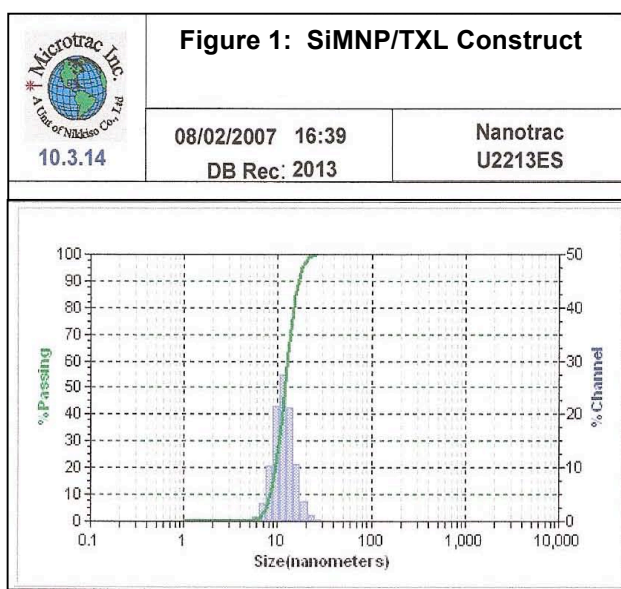
respectively, and by Vibrating Sample Magnetometry (VSM) to provide a quantitative measure of magnetic susceptibility. The magnetic susceptibility is useful for assessing the potential for MNP (~65 emu/g) and SiMNP (~45 emu/g) to be influenced by an external magnetic field.

Several parameters were considered in arriving at the choice of magnetite as the initial vectoring material for evaluation. First, the magnetic susceptibility of our synthesized SiMNP has been shown in our preliminary data to be sufficient to respond to magnetic field gradients achievable with commercially available magnet configurations. Second, while other types of magnets exist with higher magnetic moments, such as those utilizing Ni or Co, our approach eliminates the issues of carrier toxicity and difficult syntheses, allowing the focus to be on SiMNP behavior as the delivery vehicle.

Biocompatibility and hermeticity of SiMNP were assessed by several methods that assessed the potential for free radical generation, which included Electron Spin Resonance (ESR), based on the Fenton system known to generate free radicals in the presence of DMPO (5,5-dimethyl-1-pyrroline-N-oxide). Results indicated no evidence for free radical generation with our synthesized SiMNP.

To better understand SiMNP toxicity, female nude mice were injected with 150 μ L of 1000 μ g/ml solutions of FITC-labeled SiMNP and held for six months prior to sacrifice (Klostergaard et al., unpublished). Routine hematological (complete CBC and differential) and chemistry (bilirubin, electrolytes, creatinine, BUN, glucose, calcium, phosphorous, serum enzymes, LDH, and total protein) assays were conducted and did not reveal any significant alterations in the SiMNP-treated mice compared to age-matched controls. Histopathological evaluation by a board-certified veterinary pathologist was unremarkable, revealing only aging-associated alterations, not unique to the MNP-treated mice. **These results provide evidence of SiMNP biocompatibility and resistance to physiological degradation.**

SiMNP-TXL constructs, as stable nanodispersions, have also been synthesized and characterized by dynamic light scattering (**Figure 1**) to show the SiMNP-TXL construct in a narrow size distribution around 10nm diameter. Carbon analyses of the SiMNP-linker and the SiMNP-TXL construct showed 6.15 wgt % and 9.66 wgt %, respectively. SiMNP sites, fully saturated with linker moieties, based on steric assumptions, would show a maximum carbon due to TXL to be ~10% (0.5gram TXL per gram of SiMNP for a 10nm particle), after accounting for the



carbon contribution from the linker. Data developed from synthesized SiMNP constructs showed 3.5% TXL content (0.05g TXL per gram SiMNP) again after accounting for the carbon contribution from the linker. These results indicate that approximately 15% of the available sites on SiMNP (10nm diam.) were consumed by TXL, which would allow for delivery of ~15ug of TXL, a significant dose, to the tumor.

Thus, we provide evidence below that SiMNP nanomaterials used in our small animal nude mouse xenograft models were nanoscale in character and that this delivery system has the potential to target an effective dose of TXL.

In Vivo Localization of MNPs to Human Breast tumor Xenografts

To validate the feasibility of magnetically vectoring MNPs, we evaluated the concept in orthotopic human MDA-IBC-1 nude mouse xenografts. The cells for these xenografts were obtained from Dr. Wendy Woodward, MD Anderson Cancer Center. They were established from fresh pleural effusions obtained under an MD Anderson IRB-approved protocol from a patient with metastatic and therapy-resistant IBC.

Fresh pleural effusion cells and mammospheres derived therefrom were PAP stained and analyzed by a breast pathologist to confirm that growing cells were tumor and resembled the original pathology. Attached cells demonstrated tube



Figure 2: Orthotopic transplantation of MDA-IBC-1 cells resulted in tumor formation with gross skin involvement (left), gross angiogenesis

formation with mobile projections connecting foci of attached cells and had mesenchymal morphology. MDA-IBC-1 cells were transplanted in Matrigel into the cleared mammary fatpads of 3-week old Nod/Beige mice (2×10^6 cells/gland). Ten of ten injected glands developed tumors at 14 days. One tumor had gross skin change at the time of sacrifice (**Figure 2, left panel**). Most had mild/moderate erythema. All tumors had evident tumor vasculature (**Figure 2, middle panel**). H & E staining was performed and compared to the patient's original primary tumor by a breast pathologist. Histology resembled patient primary: high grade and malignant (**Figure 2, right panel**). Immunohistochemistry confirmed maintenance of initial receptor phenotypes, ER(+), PR(-), Her-2-neu(-).

To conduct the MNP localization studies, female nude mice were orthotopically (mammary fatpad) implanted with the MDA-IBC-1 cell line using matrigel, and

tumors were allowed to grow until their longest diameter reached between 4-10 mm. Then, following i.v. administration protocols, 50 ml of a 25 mg/ml solution of carboxy-silane-modified MNPs were injected with the point of a pyramid-crowned, tandem magnet (**Figure 3**) juxtaposed over the orthotopic tumor. Pre- (left panels) and post (right panels)-magnetic vectoring (magnet in place for 30 min) MR images (T1MSME, top panels; T2FSE, bottom panels) were acquired (**Figure 4**). The evidence for MNP-induced susceptibility artifacts is clear using either the T1- or T2- weighted images. There was no MR evidence for MNP localization without the magnet in place (data not shown).



Figure 3: Permanent magnet combination where the small susceptor face is juxtaposed on the mouse

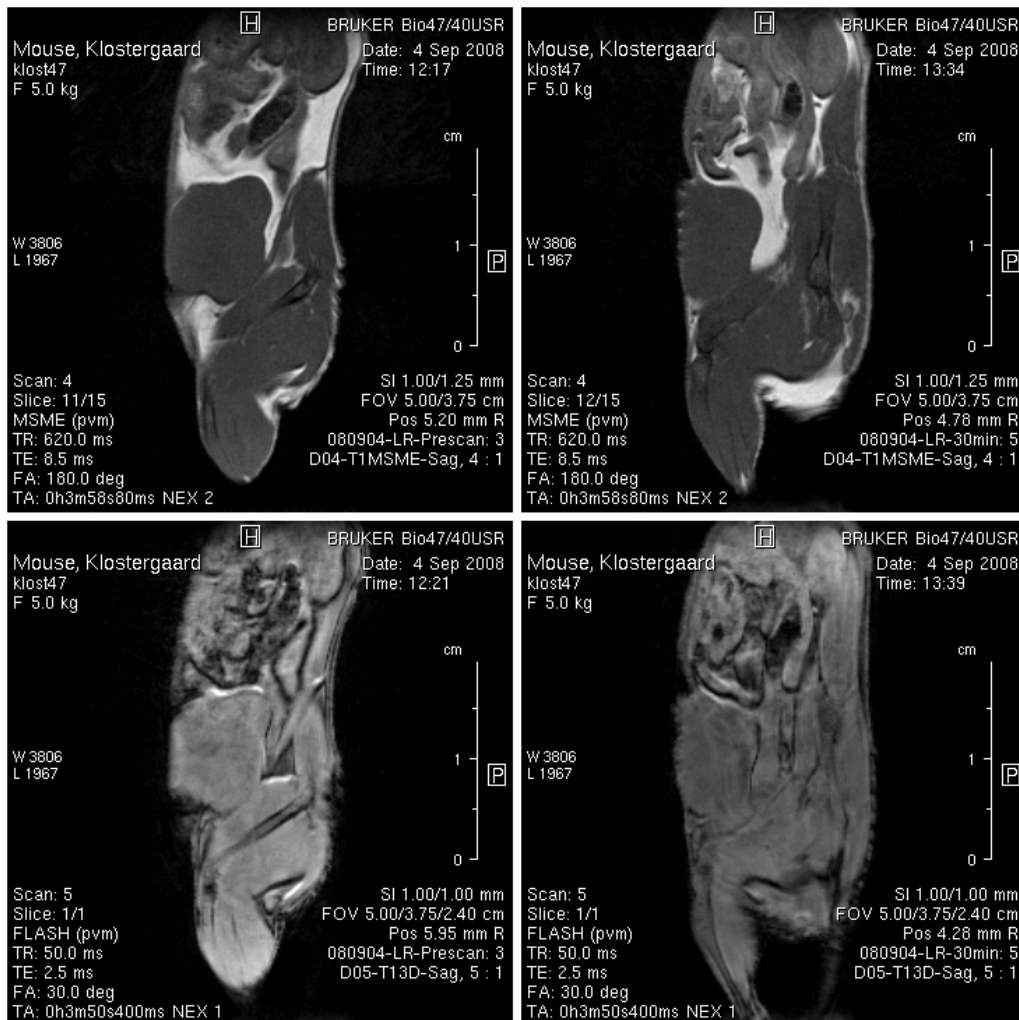


Figure 4: Pre- (left panels) and post (right panels)-magnetic vectoring (magnet in place for 30 min) MR images (T1MSME, top panels; T2FSE, bottom panels)

To begin to assess the kinetics of the retention mechanism in the IBC-1 xenograft, mice with IBC-1 tumors were subjected to the same protocol as described for the experiment in **Figure 4**, and then subjected to repeated MR imaging 24 and 48 hr later. The results are shown in **Figure 5**, and clearly demonstrate diminished signal by 24 hr, and essentially complete equivalence to pre-injection images by 48 hr, suggesting protracted clearance compared to that expected for free drugs.

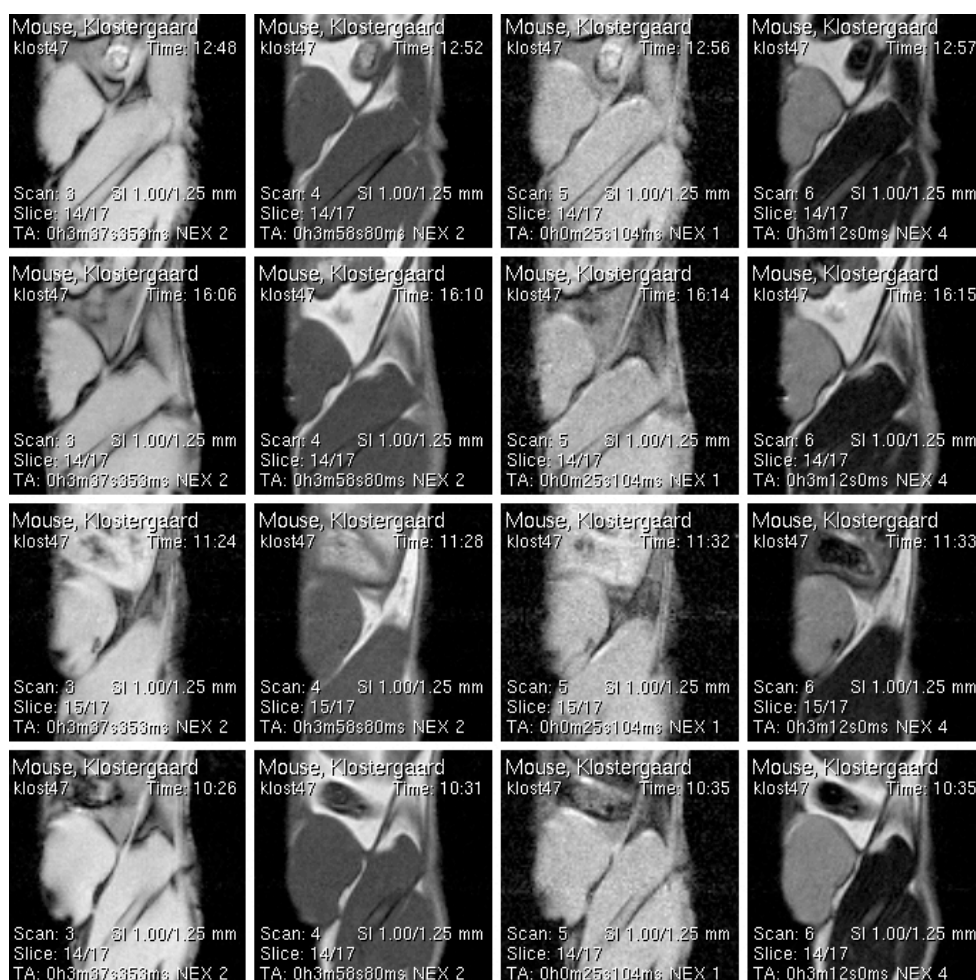


Figure 5: Top row is prescan, 2nd from top is after injection, 3rd row is +24h, bottom row is +48h. Leftmost column is lightly T2*-weighted, 2nd column from left is T1-weighted spin-echo, 3rd column is T13D gradient echo, and rightmost column is T2-weighted spin echo.

Key Research Accomplishments

- 1) Selection of six families of anti-CD44 HABD thioaptamer sequences using bead selection approach.
- 2) Synthesis and characterization of lead monodispersed MNP-TXL conjugate.
- 3) Demonstration of magnetically-enhanced localization of MNPs to human orthotopic tumor models, including breast.

Conclusions

We have been successful in achieving some key elements needed for construction of a lead anti-CD44-HABD-MNP-TXL construct, as well as in achieving localization of a parental MNP formulation to orthotopic human breast tumor xenografts. The next steps will include 1) validating HABD binding in solid-phase binding assays by the candidate anti-CD44 HABD thioaptamers; 2) if successful, subsequent analysis by competitive binding assays on CD44(+) human breast tumor cells (e.g., SKBR-3 or HBL-100); 3) synthesis of a lead conjugate of anti-CD44 HABD-thioaptamer-MNP, and repetition of the competitive binding assays performed for the free anti-CD44 HABD-thioaptamer; 4) synthesis of a lead conjugate of anti-CD44 HABD-thioaptamer-MNP-TXL and determining CD44-dependent cytotoxicity of this conjugate on CD44(+) tumor cells defined above; 5) evaluation of toxicity and anti-tumor efficacy of this lead formulation in orthotopic nude/SCID mouse human tumor xenografts.

Translation to Military Medicine

Breast cancer mortality is influenced by access to health care as well as by genetic and other factors. This is true in the civilian population, but women in the armed services should be able to access appropriate medical care, irrespective of their socio-economic status as civilians. With this technology currently under development, the desired endpoint is delivery of this therapy in an ambulatory treatment center or clinic, or at bedside if required for other reasons; we fully anticipate that this should be feasible at any sophisticated hospital offering oncology care to active or retired service personnel.

Scientific Publications, Abstracts, & Presentations

Numerous poster presentations at international meetings, including the 2006 EORTC/AACR/NCI meeting, entitled "Magnetic localization of magnetically-responsive nanoparticles to human ovarian carcinoma peritoneal xenografts", by Jim Klostergaard, James Bankson, William Yuill and Charles E. Seeney, the 2007 9th US-Japan Symposium on Drug Delivery Systems entitled "Bimodally-

targeted, magnetically-responsive nanoparticles as drug carriers”, by Jim Klostergaard, Joan Bull, David Gorenstein and Charles Seeney, and the 2008 First International Meeting on Inflammatory Breast Cancer, entitled “Localization of magnetically-responsive nanoparticles (MNPs) to orthotopic human IBC xenografts”, by Jim Klostergaard, James Bankson, Wendy Woodward, and Charles Seeney.

Funding Received as a result of the seed funds

The ANH funding helped provide preliminary data on thioaptamer development that was used to successfully renew a U54 grant between MD Anderson Cancer Center and the University of Puerto Rico Cancer Center.

Similarly, this data has been used in pending proposals, including an Ovarian Cancer SPORE Development Proposal, as well as in response to a solicitation for projects to include in the renewal of the Ovarian Cancer SPORE at MD Anderson.

PROJECT 7

Guided-Microvasculature Formation and Cellular Infiltration for Tissue Regeneration Applications in Nano-Structured Sil-Fibroin Chitosan Scaffolds

Anshu Mathur, PhD (M.D. Anderson Cancer Center)
Rebecca Richards-Kortum, PhD (Rice University)

Introduction

The attached publication addresses the introduction, results & discussion, key research accomplishments, and conclusions.

Gupta V, Davis G, Gordon A, Altman A, Reece G, Gascoyne P, **Mathur AB**, Endothelial and Stem Cell Interactions on Dielectrophoretically Aligned Fibrous Silk Fibroin-Chitosan Scaffolds, **Journal of Biomedical Materials Research**, Accepted October 2009.

- We have a novel patentable method for fabrication of 3-D nano-fibrillar scaffolds that affect endothelial and stem cell migration and adhesion and guide cells in vivo
- We have submitted for further support from the NIH as an R01. See details below. This was our last task on the timeline and we have accomplished it.
- **Principal Investigator**, Engineered Biologics for Repair of Abdominal Wall Musculofascia, NIH **R01AG034658**, National Institute on Aging (NIH/ NIA), \$1,902,141, Score 1.9, 7th percentile, **Begins April 1st, 2010**. (Co-Investigator, Charles E. Butler, Plastic Surgery)
- *For repair and reconstruction of abdominal wall musculofascia due to tumor resections and hernias. Has both basic science and translational science components.*
- *The preliminary data for this grant was obtained in combination from my NIH R21 and the nano grant from Alliance for NanoHealth/ Department of Defense TATRC funds.*

Translation to Military Medicine

The design and development of biodegradable matrices that will replace the native tissue without necrosis or scar formation is a challenging area of research. The composition, architecture, and mechanical properties of the scaffold or matrix are important criteria for bone formation due to its load bearing properties. The structural and biological characteristics also control the initial inflammatory response, cell conductivity or infiltration, generation of the neo-ECM, biodegradation of the biomaterial scaffold, mechanical properties of the remodeled or regenerated tissue, vascularization, mineralization, and

differentiation of bone cells. The critical balance that needs to be maintained in the wound healing of load bearing tissues such as bone, is that the degradation rate of the implanted biomaterial should equal the deposition of new matrix so that mechanical strength is not compromised.

The hurdles in regenerative tissue engineering can be overcome by developing structurally engineered 3-D scaffolds using biological sources whose micro and macro structure, mechanical properties, and chemical composition can be designed based on the clinical need. The present funded work provides such strategy to design regenerative biomaterials from nano to macro level per patient specific need for guided regeneration of tissues. In the military, patients that have major injuries due to trauma or other accidents in the battlefield will benefit from this research since many of these injuries are in the maxillofacial region. This work provides an unique way to promote Vascularization and guide the regeneration of critical sized defects in patients with maxillofacial injuries.

Scientific Publications, Abstracts, & Presentations

The publication resulting from this work is attached (Gupta V, Davis G, Gordon A, Altman A, Reece G, Gascoyne P, **Mathur AB**, Endothelial and Stem Cell Interactions on Dielectrophoretically Aligned Fibrous Silk Fibroin-Chitosan Scaffolds, **Journal of Biomedical Materials Research**, Accepted October 2009).

Funding Received as a result of the seed funds

We have submitted for further support from the NIH as an R01.

- Principal Investigator, Engineered Biologics for Repair of Abdominal Wall Musculofascia, NIH R01AG034658, National Institute on Aging (NIH/ NIA), \$1,902,141, Score 1.9, 7th percentile, Begins April 1st, 2010. (Co-Investigator, Charles E. Butler, Plastic Surgery)
- For repair and reconstruction of abdominal wall musculofascia due to tumor resections and hernias. Has both basic science and translational science components.
- The preliminary data for this grant was obtained in combination from my NIH R21 and the nano grant from Alliance for NanoHealth/ Department of Defense TATRC funds.

Endothelial and stem cell interactions on dielectrophoretically aligned fibrous silk fibroin-chitosan scaffolds

Vishal Gupta,¹ Greg Davis,¹ Alexander Gordon,¹ Andrew M. Altman,^{1,2} Gregory P. Reece,¹ Peter R. Gascoyne,² Anshu B. Mathur¹

¹Department of Plastic Surgery, The University of Texas, MD Anderson Cancer Center, Houston, TX

²Department of Molecular Pathology, The University of Texas, MD Anderson Cancer Center, Houston, TX

Received 27 July 2009; revised 14 October 2009; accepted 29 October 2009

Published online 00 Month 2009 in Wiley InterScience (www.interscience.wiley.com). DOI: 10.1002/jbm.a.32720

Abstract: Regenerative tissue engineering requires biomaterials that would mimic structure and composition of the extracellular matrix to facilitate cell infiltration, differentiation, and vascularization. Engineered scaffolds composed of natural biomaterials silk fibroin (SF) and chitosan (CS) blend were fabricated to achieve fibrillar nano-structures aligned in three-dimensions using the technique of dielectrophoresis. The effect of scaffold properties on adhesion and migration of human adipose-derived stem cells (hASC) and endothelial cells (HUVEC) was studied on SFCS (micro-structure, unaligned) and engineered SFCS (E-SFCS; nano-structure, aligned). E-SFCS constituted of a nano-featured fibrillar sheets, whereas SFCS sheets had a smooth morphology with unaligned micro-fibrillar extensions at the ends. Adhesion of hASC to either scaffolds

occurred within 30 min and was higher than HUVEC adhesion. The percentage of moving cells and average speed was highest for hASC on SFCS scaffold as compared to hASC cocultured with HUVEC. HUVEC interactions with hASC appeared to slow the speed of hASC migration (in coculture) on both scaffolds. It is concluded that the guidance of cells for regenerative tissue engineering using SFCS scaffolds requires a fine balance between cell–cell interactions that affect the migration speed of cells and the surface characteristics that affects the overall adhesion and direction of migration. © 2009 Wiley Periodicals, Inc. J Biomed Mater Res Part A: 00A: 000–000, 2010

Key Words: silk fibroin, stem cells, dielectrophoresis, scaffold, cell migration, nanostructure

INTRODUCTION

Cellular interactions at the molecular scale are important to elucidate the parameters necessary for complex tissue formation using biomaterials or matrices. Reconstruction and regeneration of complex tissues using biodegradable matrices requires molecularly engineered design, which can guide tissue formation without scarring and is therefore a challenging area of research. Most currently available biomaterials used in the area of reconstruction or repair are not designed to regenerate tissue but to cover or fill defects and/or perform a mechanical function. A regenerative biomaterial is defined as one that recruits wound healing and precursor cells *in vivo* to form new viable and vascularized tissue to repair or reconstruct a defect.

The composition and architecture of a regenerative biomaterial regulates the initial inflammatory response, rate of biodegradation, vascularization, cellular infiltration with stem cells, deposition of new extracellular matrix (ECM), and mechanical properties of the regenerated/remodeled tissue. We have reported that the blend of two biologically derived materials silk fibroin (SF) and chitosan (CS) meets the criteria of a regenerative biomaterial as it supports the

regeneration of muscufascia¹ and bone² in two different *in vivo* models. Therefore, with the established regenerative potential of SFCS scaffolds, in this study, we investigated the interactions of stem cells and endothelial cells in order to identify parameters for guidance of tissue regeneration using the SFCS biomaterial system.

Matrix-based guidance of cells to form structures such as blood vessels has been evidenced during *in vivo* angiogenesis, where capillary sprout endothelial cells and pericytes preferentially migrate along elastic fibers found in the ECM to form neovessels.³ The critical point to note from this study was the fact that the capillary sprout endothelial cells can use existing fibers in the ECM as substrate to guide microvascular growth. As SF is a fiber forming polymer⁴ and has shown *in vivo* regenerative capacity^{1,2} in our previous studies, we used the technique of dielectrophoresis to organize the structure of SFCS scaffolds at the nanoscale in three dimensions (3-D) similar to the ECM.

Previously, dielectrophoretic forces have been used for the manipulation of microparticles and cells,^{5,6} collection of macromolecules,⁷ nanoparticles,⁸ and nanotubes.⁹ Nanofibrous structures of various compositions have been shown

Correspondence to: A. B. Mathur; e-mail: amathur@mdanderson.org

Contract grant sponsor: High Resolution Electron Microscopy Facility, UTMDACC; contract grant number: #CA16672

Contract grant sponsor: National Science Foundation; contract grant number: #0335765

Contract grant sponsors: Department of Defense—Telemedicine and Advanced Technology Research center, Gilsson Logenburgh Foundation, Anderson Foundation and Alliance for Nanohealth, Houston, Texas

to have many applications in tissue engineering, biomedicine, and biotechnology.^{10,11} In this study, the use of dielectrophoresis to achieve the formation and alignment of SF fibrils within a 3-D scaffold and the scaffold properties for the guidance of cells was investigated.

The interactions of human adipose tissue derived stem cells (hASC) with the SFCS scaffold and the delivery of these cells *in vivo* for wound healing was recently explored by our group.^{12,13} In this study, we investigated and compared the adhesion and migration behavior of hASC and human umbilical vein endothelial cells (HUVEC) on engineered scaffolds (E-SFCS) with aligned nanofibers in a 3-D architecture and our conventional first generation scaffolds (SFCS)¹⁴ that had features of smooth sheets with microfibril extensions. This is the first study to use the technique of dielectrophoresis to fabricate scaffolds with SF fiber alignment in 3-D and compare the HUVEC-hASC interactions on two scaffolds with the same composition but different morphological features.

MATERIALS AND METHODS

Silk fibroin and chitosan scaffold preparation

Raw silk was obtained from the Korean Sericulture Institute and originated from Sau Paulo, Brazil (Kindly donated by Dr. Sam Hudson, North Carolina State University, Raleigh, NC). High molecular weight CS (82.7% deacetylation) was obtained from Sigma-Aldrich (St. Louis, MO). The blend of 75:25 SF and CS was prepared as described previously.¹⁴ Briefly, raw silk was degummed (removal of sericin coating) in 0.25% (w/v) sodium carbonate and 0.25% (w/v) sodium dodecylsulfate (Sigma-Aldrich) for 1 h at 100°C. The degummed silk (SF) was then dissolved in calcium nitrate tetrahydrate and methanol solution (molar ratio of 1:4:2 Ca:H₂O:MeOH) at 65°C. CS was dissolved in 2% acetic acid solution at the same concentration as SF solution and was mixed together in a ratio of 1:3 (1 part CS and 3 parts SF) to prepare 75:25 SFCS. The SFCS scaffolds (controls, unaligned, micro-fibrils) were prepared by freezing 75:25 SFCS blend at -80°C overnight and then lyophilizing for 24 h. The dry scaffolds were treated with 50:50 (v/v) methanol:sodium hydroxide (1 N) solution for 15 min to crystallize the SF and neutralize remaining acidity of the chitosan. Later the scaffolds were left overnight in 1 N sodium hydroxide solution. The scaffolds were washed several times in phosphate buffer saline (PBS) solution (Lonza, Walkersville, MD) to equilibrate the pH to 7.0. The SFCS scaffolds were sterilized in ethanol solution (70%) overnight under the laminar flow hood and again washed with PBS several times to bring the pH equal to 7.0.

E-SFCS preparation using dielectrophoresis

E-SFCS scaffolds were prepared using dielectrophoresis technique.⁵ The electrodes were interdigitated triangular castellations arrays of gold on top of a glass microscope slide, and were fabricated using UV photolithography and

F1

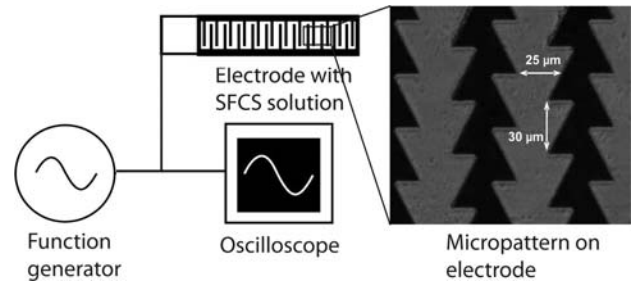


FIGURE 1. Images of the dielectrophoresis technique (left) and triangular castellations on micropatterned electrode (right).

Arbitrary Waveform Generator), and a 100 kHz, 10 V(p-p) sine wave was applied across the sample for 45 min (Fig. 1). The electrode voltage, field frequency, and time were optimized for better alignment of SF fibers. The fibers collect to the electrode tips of the triangular micropattern and move to the gaps by repulsion of fibers. The scaffold was then frozen in liquid N₂ vapors and lyophilized. E-SFCS scaffold was then crystallized and sterilized as mentioned earlier for SFCS scaffolds.

The model of self assembly of SF fibrils in 3-D SFCS scaffold using dielectrophoresis is described as-

If a rod-shaped particle is placed in an inhomogeneous alternating electric field, it will experience a time-averaged, translational dielectrophoretic force due to induced dipolar effects¹⁵⁻¹⁸ given by-

$$\vec{F}_{DEP} = \frac{\pi a^2 b}{3} \epsilon_m f_{CM} \nabla |\vec{E}|^2 \quad (1)$$

Where, 'a' is the radius of the rod and 'b' is its length. ϵ_p^* and ϵ_m^* are the complex permittivities of the particle and its suspending medium, respectively, and $\nabla |\vec{E}|^2$ is the gradient of the magnitude of the electric field squared. f_{CM} is the so-called Clausius-Mossotti factor which describes the frequency-dependent dielectric characteristics of the particle and its suspending medium,

$$f_{CM} = \text{Re} \left\{ \frac{\epsilon_p^* - \epsilon_m^*}{\epsilon_p^* + 2\epsilon_m^*} \right\} \quad (2)$$

Quadrupole and higher dielectric terms, ignored here, may be included if required.¹⁶⁻¹⁸ Equation (2) shows that the dielectrophoretic force is attractive or repulsive depending on whether the polarizability of the particle is greater or less than that of its suspending medium, respectively. The complex permittivity of a particle may be expressed in terms of core dielectric (ϵ_p), core conductivity (σ_p), and surface (interfacial) conductivity (K_s) properties as $\epsilon_p^* = \epsilon_p - \frac{j}{\omega} (\sigma_p + \frac{2K_s}{a})$, where $j = \sqrt{-1}$ and ω is the angular frequency of the applied electric field.¹⁹ Even when the particle core is less polarizable than the suspending medium, the surface conductivity term will overwhelm the intrinsic particle properties and lead to attractive dielectrophoretic forces below some crossover frequency at which $\text{Re}(f_{CM}) = 0$. Solving Eq. (2) for this condition yields

$$\omega = \left[\frac{\left(\frac{2K_s}{a} + \sigma_p - \sigma_m \right) \left(\frac{2K_s}{a} + \sigma_p + 2\sigma_m \right)}{(\epsilon_m - \epsilon_p)(\epsilon_p + 2\epsilon_m)} \right]^{\frac{1}{2}} \quad (3)$$

Of significance to the molecular assembly work proposed here for elongating silk proteins is that the radius of the particle, a , affects the contribution made by surface conductivity to the magnitude and sign of the dielectrophoretic force. To illustrate this, the crossover frequency is plotted at right for aqueous solutions of 1 to 16 mS/m conductivity, a core protein dielectric constant of $4\epsilon_0$, and a surface conductivity of 2 nS, as a function of particle radius (Fig. 2). The plot shows that small radius (<100 nm) molecules experience dielectrophoretic attraction to electrode tips even at high frequencies. However, the crossover frequency decreases sharply and becomes negative if molecular assembly into solid fibers of sufficiently large radius occurs. The threshold radius for which the crossover frequency drops off rapidly is determined by the suspension medium conditions. This shows that it should be possible to concentrate and orient small radius, elongate molecules by strong attractive dielectrophoretic forces at the electrode tips yet repel larger radius assembly products toward low field regions between the electrodes. Once focused and oriented in low field regions, additional assembly to form much larger structures can proceed. The advantages of this scheme are that a continuous assembly process is enabled in which the electrode tips remain clear of assembled material and in which very large fibers can be assembled in extensive, oriented “bay” regions between rows of electrode tips. In this way, the scale of the assembled fibers may be significantly larger than the scale of the electrode tips. This methodology provides the possibility of creating oriented fiber assemblies in 3-D through repulsion from two-dimensional (2-D) electrode planes because, while positive dielectrophoresis depends on high field regions that can only be produced at localized structures, negative dielectrophoresis can concentrate matter away from structures and surfaces.

Cell culture

hASC were obtained from InGeneron Inc. (Houston, TX) and cultured in α -minimum essential medium (Gibco, Grand Island, NY) containing 20% fetal bovine serum, 2 mM L-glutamine, 100 U/mL penicillin, and 100 μ g/mL streptomycin.^{13,20} HUVEC were obtained from Cascade Biologics (Portland, OR) and cultured in Medium 200 containing low serum growth supplements (Cascade Biologics). Both hASC and HUVEC were cultured at 37°C in 100% humidified atmosphere with 5% CO₂ supply. Passages from 3 to 6 were used for both cell types in all the experiments.

Polarized light microscopy

SFCS and E-SFCS were imaged using polarizer, crossed-analyzer, and a red retardation plate ($\lambda = 530$ –560 nm) attached to Olympus IX70 (Olympus, Center Valley, PA) microscope. Polarized light microscopy was used to assess

the alignment and orientation of the fibrils within the scaffold.

Scanning electron microscopy (SEM)

SFCS and E-SFCS scaffolds were cut (6 mm diameter) to fit 96-well cell culture plate and kept at the bottom of the plate. The scaffolds were seeded with 300,000 cells (hASC or HUVEC or both cell types together) per well and incubated for 30 min at 37°C. The scaffolds were washed two times with PBS to remove unattached cells and then fixed in 2% paraformaldehyde and 3% glutaraldehyde solution. Unattached cells were counted to calculate the percent adhesion of cells to scaffolds. The cell-seeded scaffolds were imaged using JSM-590 scanning electron microscope (JEOL, USA, Inc., Peabody, MA) as described before.¹²

Cytokinetic study using time-lapse confocal microscopy

The hASC were transfected with green fluorescent protein (GFP) using lentiviral construct as described previously.^{21,22} Briefly, 1 million cells were infected with lentiviral construct and cultured in CMV-eGFP lentivirus-containing medium (1.2 million virus particles/mL medium) with 8 μ g/mL polybrene (Sigma-Aldrich, St. Louis, MO). GFP-positive cells were later sorted using FACSVantage SE cell sorter (Becton-Dickinson, Franklin Lakes, NJ) and cultured in α -minimum essential medium as earlier. HUVEC were labeled with DiI dye (Invitrogen, Carlsbad, CA), which bind to cell membrane. First, 2 million HUVEC were suspended in 2 mL of Hanks Balanced Salt solution (Lonza) and 0.5 μ L of DiI (from 10 mg/mL DiI stock in EtOH) was added in dark. Both hASC and HUVEC were also labeled for nucleus stain using Hoechst dye (Sigma-Aldrich; 5 μ g per million cells). After the addition of dyes under limited light conditions, the cell suspension was incubated at 37°C for 5 min then at 4°C for 15 min and again at 37°C for 30 min ending with 30 min at room temperature. The cell suspension was centrifuged at 1500g for 10 min and the pellet was suspended in the culture medium. The ethanol-sterilized E-SFCS and SFCS scaffolds were cut and kept at the bottom of 96-well plate. Fluorescently labeled hASC and HUVEC (total 100,000 cells per well) were seeded on top of scaffolds either single or in coculture. After 30 min, unattached cells were washed with PBS and the cell-seeded scaffolds were imaged using confocal fluorescence microscope Olympus IX81 (Olympus, Center Valley, PA, USA) every 15 min for 4 h. Later, the images were processed for cytokinetic data calculations (cell speed and persistence time) using Slidebook software (Intelligent Imaging Innovations GmbH, Göttingen, Germany). Persistence time is the length of time before the cell changes its direction of movement significantly.^{23,24} The “average speed” of the cell and “persistence time” are the parameters used commonly to analyze the cell migration on a particular substrate. As not all focus areas (frames) during time-lapse confocal microscopy imaged moving cells, we captured more than one frame on a single sample.

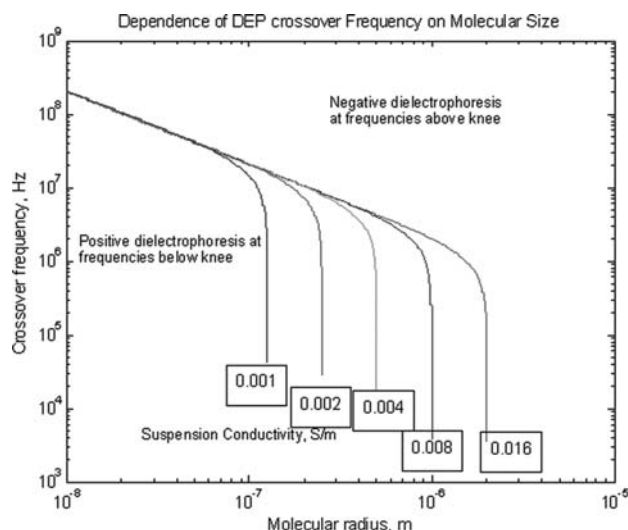


FIGURE 2. Plot of crossover frequency versus particle radius for aqueous solutions of 1 to 16 mS/m conductivity, a core dielectric constant of 4, and a surface conductivity of 2 nS in order to illustrate the self-assembly of silk fibroin and chitosan polymers in to fibrils under dielectrophoretic forces. [Color figure can be viewed in the online issue, which is available at www.interscience.wiley.com.]

Statistical analysis

The data was compared statistically using SigmaStat program. The level of significance was chosen as $p < 0.05$. Two-way ANOVA was performed with scaffold type (E-SFCS versus SFCS) as factor 1 and cell type (hASC versus HUVEC) as factor 2 to analyze the results of adhesion and migration. Also, *post hoc* Tukey test was used for pair-wise comparison.

All data was represented as mean \pm standard error of mean.

RESULTS

Comparison of SFCS and E-SFCS scaffold morphology

SF fibril and polymer chain alignment within the fibril was studied previously using polarized light microscopy using a polarizer, analyzer, and a red retardation plate [Fig. 3(A)].⁴ Under the polarizer-analyzer with no red plate, the white aligned fibrils embedded in the black are observed, where white regions indicate alignment of polymer chains within the SF fibrils and black areas are unaligned regions of the SFCS scaffold [Fig. 3(B)]. Fibrils showed distinct alignment at 45° angle to the electrode bars. Under the red retardation plate, SF polymer chains distinctly reflect blue showing that polymer chains within the fibrils aligned primarily parallel to the fibril direction [Fig. 3(C)]. As fiber assemblies begin to grow in thickness and length, their dielectric properties change and they are repelled into the gaps between electrodes where they assemble into larger fibers (~50 μ m) that are aligned along the negative dielectrophoretic regions. Moving along the z-axis of the assembled scaffold, it was observed that the E-SFCS was composed of layered sheets of aligned fibers. However, SFCS scaffold showed no such alignment of fibrils as previously reported.¹⁴ The surfaces of E-SFCS sheets [Fig. 4(A)] were featured with nanofibers (97.2 \pm 2.7 nm) and ridges (0.51 \pm 0.03 μ m) whereas the surface of SFCS scaffold was smooth with micro projections on the edges [Fig. 4(B)] as determined with the SEM image analysis. Higher magnification images of Figure 4(A,B) are

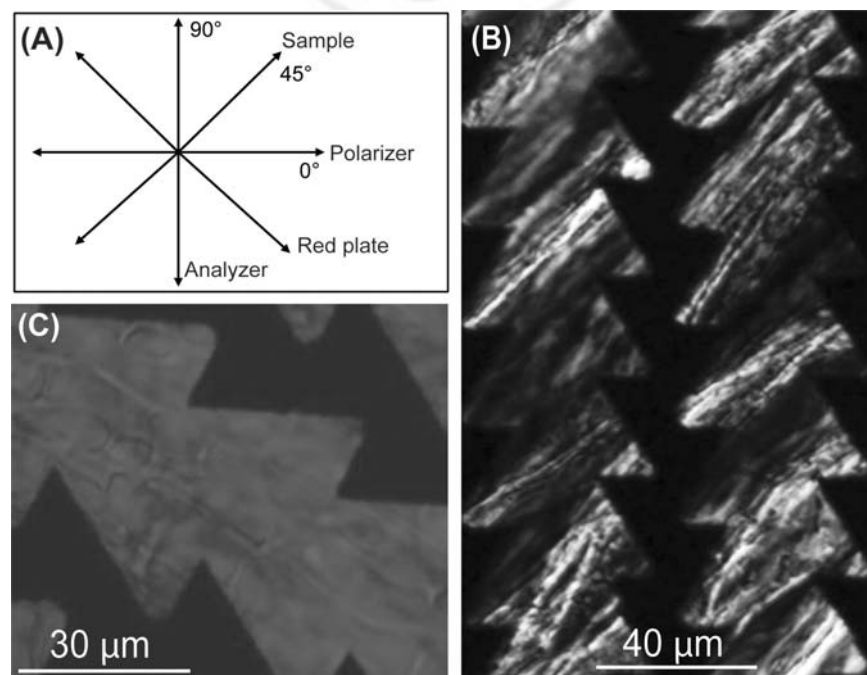


FIGURE 3. A: Schematic of polarizer and analyzer positions. B: Brightfield light microscopic image of E-SFCS showing parallel fibers. C: Polarized light microscopic image of E-SFCS. Parallel fibers are visible as blue. [Color figure can be viewed in the online issue, which is available at www.interscience.wiley.com.]

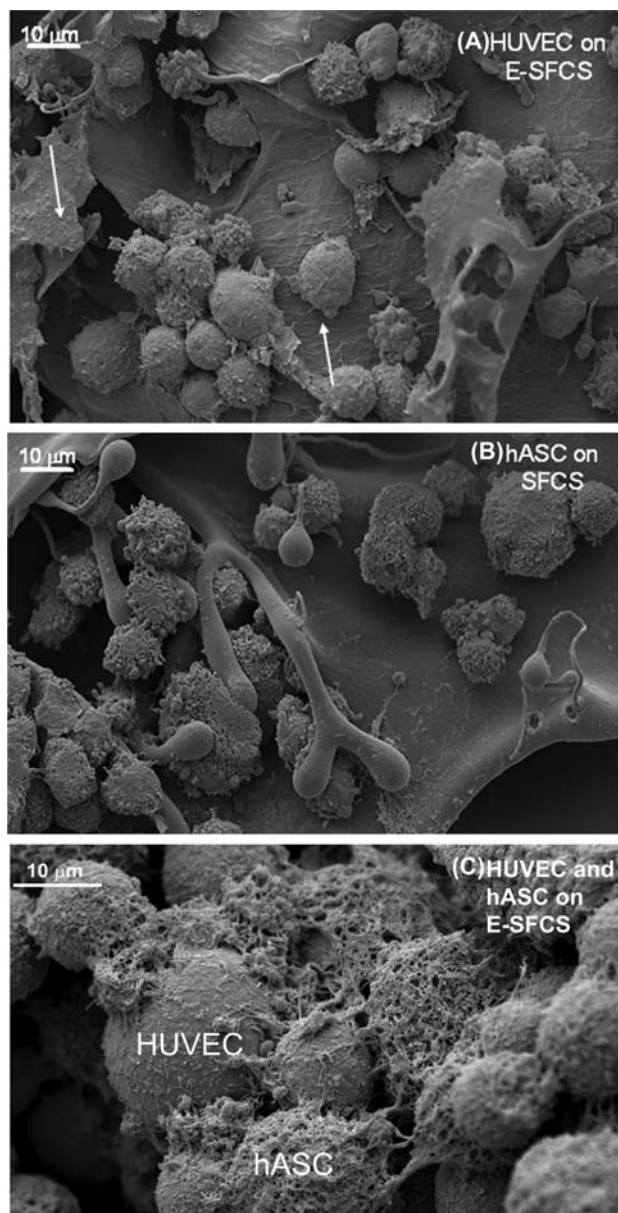


FIGURE 4. Representative SEM images of cell-seeded scaffolds. A: Single-culture HUVEC seeded on top of E-SFCS, arrow indicates the nanofibers and ridges on scaffold surface. B: Single-culture hASC seeded on top of SFCS. C: Coculture of HUVEC and hASC seeded on E-SFCS scaffold showing the interactions of HUVEC-HUVEC and HUVEC-hASC through cell extensions.

F5 also shown in Figure 5 for enhanced view of scaffold morphology.

Endothelial and stem cell adhesion to SFCS and E-SFCS scaffolds

Both HUVEC and hASC adhered to SFCS and E-SFCS scaffolds within 30 min (Fig. 4). Although the cells interacted with the nanofeatures of E-SFCS surface [Fig. 4(A)], the larger microfibrillar extensions of the SFCS captured the relatively smaller cells at the edges of the scaffold as the sur-

face of the SFCS was comparatively smooth [Fig. 4(B)]. The surface of HUVEC appeared to be smoother than the porous and hairy surface of hASC. In coculture of HUVEC and hASC, HUVEC-HUVEC, and HUVEC-hASC interacted via cellular extensions [Fig. 4(C)]. Figure 5 shows the high magnification view of the cells adherent to the nanostructured surface of E-SFCS [Fig. 5(A)] and the smooth surface of SFCS [Fig. 5(B)]. More than 85% cells adhered to the scaffolds within 30 min of incubation on both scaffold types (Fig. 6). Percent adhesion of hASC to SFCS ($98.7\% \pm 0.3\%$) and E-SFCS ($96.3\% \pm 0.7\%$) scaffolds was significantly higher ($p < 0.05$) than HUVEC on SFCS ($91.7\% \pm 1.8\%$) and E-SFCS ($89.7\% \pm 2.7\%$). However, there was no significant difference in the overall percentage of adherent cells between SFCS and E-SFCS scaffolds.

F6

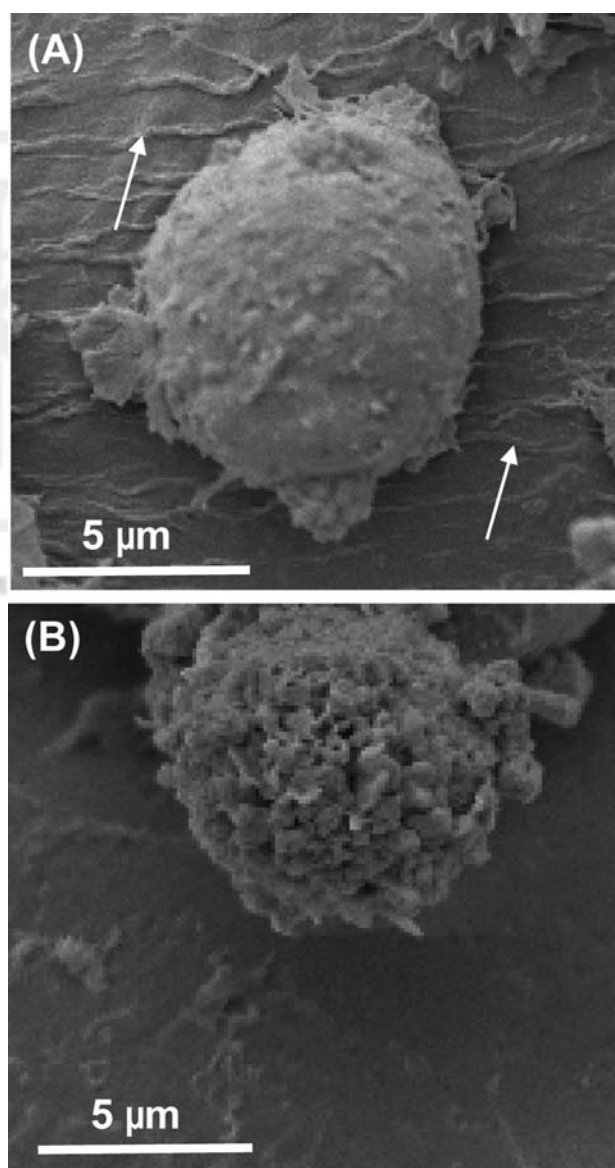


FIGURE 5. High magnification images of cells seeded on (A) E-SFCS, where the arrow indicates the nanofibers and (B) SFCS showing the morphology of the scaffolds.

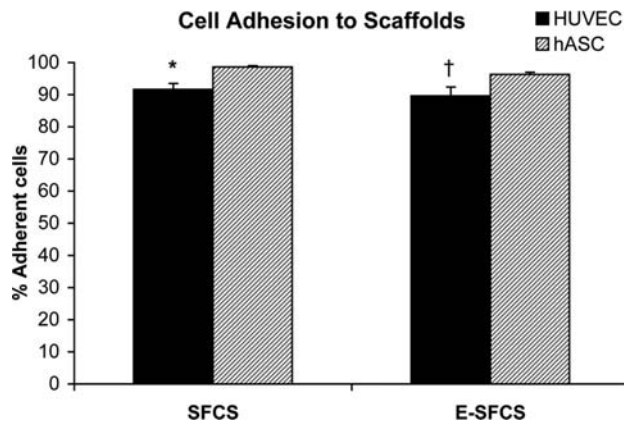


FIGURE 6. Percentage adherence of HUVEC and hASC on SFCS and E-SFCS scaffolds after 30 min of seeding ($n = 3$). * $p < 0.05$ vs. hASC on SFCS, † $p < 0.05$ vs. hASC on E-SFCS.

Endothelial and stem cell migration and kinetics on SFCS and E-SFCS scaffolds

Cells migrate on both SFCS and E-SFCS scaffolds as a function of time. Cell movement was tracked over time (up to 4 h) as shown in Figure 7 and the video can be viewed at <http://video.google.com/videoplay?docid=4866859754121817448>.

T1 Table I shows the cytokinetic data collected after cell tracking. The average speed was highest for single-culture hASC adherent to SFCS ($18.5 \pm 9.3 \mu\text{m/h}$) and was significantly higher than single-culture HUVEC ($p < 0.001$), coculture HUVEC ($p < 0.001$), and co-culture hASC ($p < 0.001$) adherent to SFCS surface. Similarly, on the E-SFCS scaffold the average speed was higher ($p < 0.1$) for single-culture hASC than co-culture hASC. Interestingly, the speed of single culture hASC was higher ($p < 0.05$) on SFCS than E-SFCS. Persistence times of the cells were comparable on either type of scaffolds except for coculture HUVEC, which was significantly lower ($p < 0.05$) on E-SFCS (13.4 min) than SFCS scaffold (35 min).

Percentage of moving cells in each image frame during 4 h of imaging time was also calculated. The percentage of moving cells was highest for single-culture hASC ($40.3 \pm 5.6\%$) as compared to single-culture HUVEC ($p < 0.05$), co-



FIGURE 7. Confocal fluorescence microscope image of cells moving on top of SFCS scaffold. hASC are labeled green and HUVEC as blue with red cell membrane. The movement of cells was tracked as shown by the tracking lines. [Color figure can be viewed in the online issue, which is available at www.interscience.wiley.com.]

culture HUVEC ($p < 0.05$), and coculture hASC ($p < 0.001$), when adherent to SFCS scaffold. In contrast, percentage of moving single and coculture HUVEC and hASC adherent to E-SFCS scaffolds showed no significant difference amongst these groups. However, percent of moving cells for single-culture hASC ($p < 0.01$) and coculture HUVEC ($p < 0.05$) were significantly lower on E-SFCS as compared to SFCS scaffold.

When both cell types were grouped together to compare differences between surfaces and assess overall cellular adhesion and migration. The persistence time was found to be significantly higher ($p < 0.05$) for cells adherent to SFCS (34.9 ± 3.2 min) as compared to E-SFCS (27.7 ± 3.6 minutes) [Fig. 8(A)]. Similarly, the percentage of moving cells was significantly higher ($p < 0.05$) for cells adherent to SFCS ($10.4 \pm 2.4\%$) as compared to E-SFCS ($4.1 \pm 1.9\%$) [Fig. 8(B)]. However, even after grouping the cell type, average speed of the cells was not significantly different when adherent to either SFCS or E-SFCS [Fig. 8(C)].

F8

TABLE I. Cytokinetic Data for Cell-Seeded SFCS and E-SFCS Scaffolds

Scaffold Type	Cell Type and Culture	Average Speed ($\mu\text{m/h}$)	Persistence Time (min)	% of Moving Cells (Image Frames)
SFCS	Single-culture HUVEC ($n = 3$)	$1.3 \pm 0.7^*$	46.7 ± 6.7	$3.6 \pm 2.2^{**}$ (3)
	Single-culture hASC ($n = 12$)	18.5 ± 9.3	41.4 ± 24.7	40.3 ± 5.6 (3)
	Co-culture HUVEC ($n = 18$)	$3.1 \pm 0.5^*$	35.2 ± 4.7	$11.5 \pm 3.8^{**}$ (23)
	Co-culture hASC ($n = 8$)	$2.0 \pm 0.3^*$	23.9 ± 2.7	$5.8 \pm 3.0^*$ (23)
E-SFCS	Single-culture HUVEC ($n = 4$)	5.1 ± 2.2	28.9 ± 8.7	6.0 ± 2.3 (4)
	Single-culture hASC ($n = 6$)	$11.1 \pm 3.7^{**}$	37.9 ± 5.2	$5.4 \pm 3.0^\dagger$ (3)
	Co-culture HUVEC ($n = 3$)	3.6 ± 0.6	$13.4 \pm 0.8^\ddagger$	$0.74 \pm 0.74^\ddagger$ (15)
	Co-culture hASC ($n = 3$)	1.8 ± 0.6	19.8 ± 1.8	6.7 ± 4.5 (15)

Data is represented as mean \pm SEM.

* $p < 0.001$ vs. single culture hASC on SFCS.

** $p < 0.05$ vs. single culture hASC on SFCS.

† $p < 0.01$ vs. single culture hASC on SFCS.

‡ $p < 0.01$ vs. single culture hASC on SFCS.

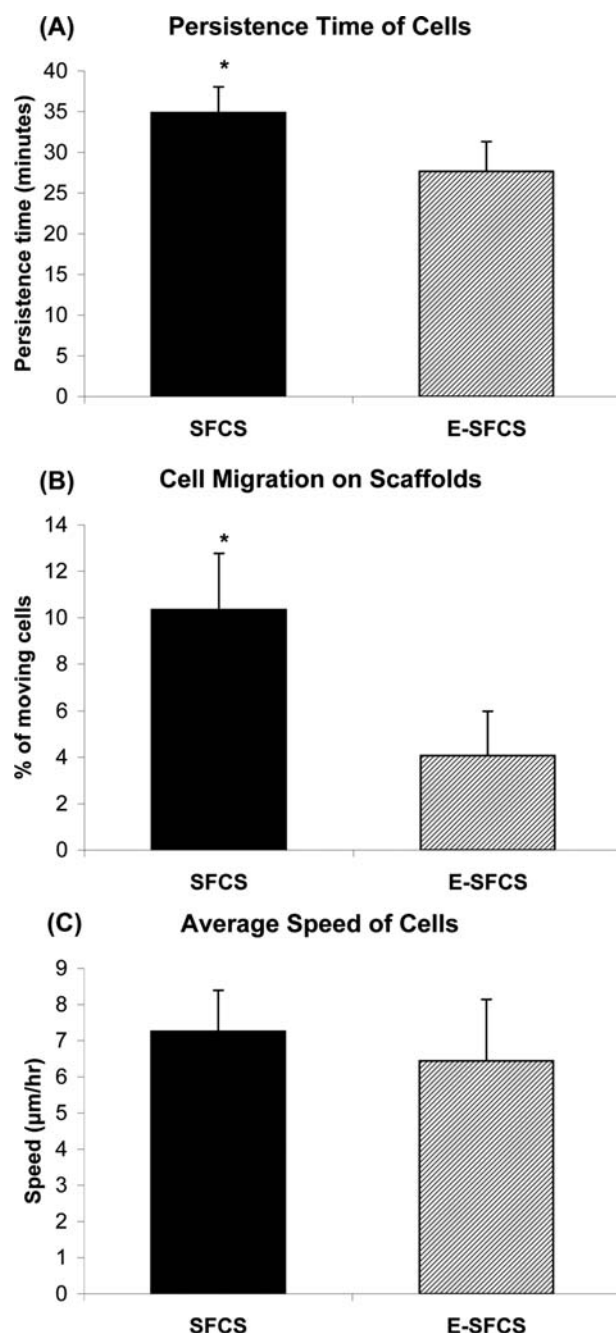


FIGURE 8. Cytokinetic data after combining hASC and HUVEC both in single and co-culture on SFCS and E-SFCS scaffolds during 4 h of fluorescence imaging. * $p < 0.05$ vs. E-SFCS.

DISCUSSION

In this study, the technique of dielectrophoresis was used for the first time to engineer SFCS scaffolds with aligned SF fibrils and nano-featured architecture self assembled in 3-D in order to investigate endothelial cell and stem cell interactions for regenerative medicine applications. The cell migration study showed that the nano-fibrillar architecture of the E-SFCS surface promoted adhesion, which slowed the migration of stem cells. Additionally, HUVEC in co-culture with stem cells slowed the migration of stem cells regardless of

the scaffold architecture. Overall, while the surface characteristics appear to affect the adhesion and direction of migrating cells, the speed of these cells appear to be more influenced by cell-cell interactions.

Percentage of moving cells (within 4 h time frame) was lower on the E-SFCS as compared to the SFCS surface for both cell types suggesting more adherent surface of E-SFCS [Fig. 8(B)]. Nanofibrous substructures on the E-SFCS surface appear to provide a fertile anchoring surface and high surface to volume ratio for enhanced cell adhesion as suggested by previous studies.¹¹ Previous studies showed that cell-substrate adhesiveness also affect the migration speed through integrin binding.²⁵ We also found that the speed of hASC reduced significantly on E-SFCS than SFCS scaffolds. It has been recently reported that HUVEC express more adhesion molecules such as $\beta 1$ -integrin on nano-fibrous pure SF nets as compared to micro-fibrous SF net scaffolds.²⁶ HUVEC prefer to adhere to the nanostructured surface of the E-SFCS also, however, in the presence of hASCs the ones that migrate tend to change their directions faster on nano-fibrous surface as compared to the smooth surface of SFCS. This peculiar behavior may be a result of the mixed cues provided by the aligned nanofibrous surface of E-SFCS and hASCs and may show an interesting HUVEC property as it balances the two cues for guided migration along the length of the nanofibers. Human endothelial cells on 2-D polystyrene surface coated with 1% gelatin have been shown to migrate at a speed of $30 \mu\text{m/h}$,²⁷ which is much higher as compared to that observed for HUVEC on SFCS ($1.3 \mu\text{m/h}$) and E-SFCS ($5.1 \mu\text{m/h}$) scaffolds. The 3-D scaffolds as compared to 2-D polystyrene surface may provide higher affinity surface to HUVEC and hASC, hence relatively lower migration speed as is evident in the difference between fewer percentage of moving cells on E-SFCS than SFCS scaffolds, with E-SFCS perhaps providing a more adhesive surface due to its nanofeatures.²⁴ Various other cell types on different surfaces have been shown to have speed in the range of 10 – $138 \mu\text{m/h}$ and persistence time in the range of 27 – 300 min .¹² The persistence time for cells in this study was in the range of 13 – 47 minutes and the average speed was 1.3 – $18.5 \mu\text{m/h}$, which were comparatively lower than other studies. Again, these lower values in our study may be because of the 3-D architecture and the biological composition of the SFCS scaffolds as opposed to the 2-D systems composed of synthetic material or gels used in other studies. To our knowledge, this is the first study to investigate the cytokinetic parameters like cell migration speed and persistence time on nano-structured scaffolds.

The migration speed was found to be the highest among all groups for hASC on SFCS scaffold, however in the presence of HUVEC in coculture, the migration speed reduced significantly. HUVEC are known to be quiescent cells unless activated by an extracellular signal such as hypoxia, stretch, or a biochemical. We observed in SEM and confocal microscopy images that HUVEC actively interact with hASC via cellular extensions. In coculture, inter-cellular signaling may allow HUVEC to communicate with hASC and reduce their speed of migration. A limitation in this cell migration study

was the shorter time capture (only up to 4 h) of cytokinetic data due to the leaching and bleaching of fluorescent dyes at longer times.

SEM images confirmed that the surface of E-SFCS scaffold was textured with nano-fibers, whereas the surface of SFCS scaffolds was very smooth with micro-projections on the edge of the sheets as was reported previously.¹⁴ In another study, we reported that more hASC attach to the micro-projections of the SFCS scaffold as compared to smoother sheet surface of the SFCS scaffold.¹² Similarly, this study showed that more cells attached to nanofibrous surface of the E-SFCS scaffold as compared to the smooth surface of the SFCS scaffold. The fibrillar morphology of the SF and CS derived scaffolds whether it was micro or nano promoted adhesion of cells. The overall affinity of cells can be rated as smooth SFCS < micro SFCS < nano SFCS. A limitation of the study was the difference in thickness of E-SFCS scaffolds produced via dielectrophoresis as compared to the SFCS scaffolds produced using conventional techniques. Increasing the thickness of the E-SFCS scaffold compromised the alignment of fibrils due to electrode design, although this is a parameter that can be altered and designed as needed per application.

The percentage of adherent cells to either type of scaffolds in 30 min was higher for hASC than HUVEC probably due to the higher surface area provided by the relatively rough/textured extracellular surface of the hASC as compared to the relatively smoother surface of the HUVEC. Interestingly, the overall cellular adhesion of HUVEC and hASC was similar on SFCS and E-SFCS, regardless of structural differences.

CONCLUSIONS

Dielectrophoresis was successfully used to engineer the SFCS scaffolds with aligned nanofiber morphology. Both SFCS and E-SFCS scaffolds facilitates hASC and HUVEC adherence, migration, and interactions although to variable extent. More cells migrate with higher persistence time on SFCS than E-SFCS. HUVEC appear to slow the speed of hASC migration on scaffolds due to cell-cell interactions whereas the surface characteristics affect adhesion and direction of migration. Hence, guidance of cells for the purpose of complex tissue formation may require manipulation of cellular interactions with its substrate at the nanoscale and E-SFCS may provide such a scaffold for tissue regeneration, though cell-cell interactions such as HUVEC-hASC play a synergistic role with surface characteristics, and has to be balanced. Therefore, a balance of sub-structural features and cell-cell interactions has to be interplayed when dealing with stem cells *in vivo* to reach complete control of the regenerative process, where a regulated regeneration is reached and unregulated growth is minimized in tissue engineered scaffolds.

ACKNOWLEDGMENTS

The authors would like to thank Dr. Jared K. Burks for helping in cytokinetic data capture and Kenneth Dunner Jr. for processing the SEM samples. Also, the assistance of Tom Anderson in

designing the mask of the micro-patterned electrode is gratefully acknowledged. Micropattern electrodes were prepared at the Microelectronics Research Center at UT Austin of National Nanofabrication Infrastructure Network.

REFERENCES

- Gobin AS, Butler CE, Mathur AB. Repair and regeneration of the abdominal wall musculofascial defect using silk fibroin-chitosan blend. *Tissue Eng* 2006;12:3383-3394.
- Rios CN, Skoracki RJ, Miller MJ, Satterfield WC, Mathur AB. In vivo bone formation in silk fibroin and chitosan blend scaffolds via ectopically grafted periosteum as a cell source: A pilot study. *Tissue Eng* 2009;15.
- Anderson CR, Ponce AM, Price RJ. Immunohistochemical identification of an extracellular matrix scaffold that microguides capillary sprouting in vivo. *J Histochem Cytochem* 2004;52:1063-1072.
- Mathur AB, Tonelli A, Rathke T, Hudson S. The dissolution and characterization of *Bombyx mori* silk fibroin in calcium nitrate-methanol solution and the regeneration of films. *Biopolymers* 1997;42:61-74.
- Gascoyne PR, Vykoukal J. Particle separation by dielectrophoresis. *Electrophoresis* 2002;23:1973-1983.
- Wang XB, Yang J, Huang Y, Vykoukal J, Becker FF, Gascoyne PR. Cell separation by dielectrophoretic field-flow-fractionation. *Anal Chem* 2000;72:832-839.
- Chou CF, Tegenfeldt JO, Bakajin O, Chan SS, Cox EC, Darnton N, Duke T, Austin RH. Electrodeless dielectrophoresis of single- and double-stranded DNA. *Biophys J* 2002;83:2170-2179.
- Morgan H, Hughes MP, Green NG. Separation of submicron bio-particles by dielectrophoresis. *Biophys J* 1999;77:516-525.
- Krupke R, Hennrich F, Lohneysen H, Kappes MM. Separation of metallic from semiconducting single-walled carbon nanotubes. *Science* 2003;301:344-347.
- Venugopal J, Ramakrishna S. Applications of polymer nanofibers in biomedicine and biotechnology. *Appl Biochem Biotechnol* 2005;125:147-158.
- Smith LA, Ma PX. Nano-fibrous scaffolds for tissue engineering. *Colloids Surf B Biointerfaces* 2004;39:125-131.
- Altman AM, Rios CN, Alt EU, Mathur AB. A silk fibroin-chitosan matrix fosters attachment and migration of human tissue resident mesenchymal stem cells. *Acta Biomater* 2009. Submitted for publication.
- Altman AM, Yan Y, Matthias N, Bai X, Rios CN, Mathur AB, Song Y, Alt EU. IFATS Series: Human adipose-derived stem cells seeded on a silk fibroin-chitosan scaffold enhance wound repair in a murine soft tissue injury model. *Stem Cells* 2008.
- Gobin AS, Froude VE, Mathur AB. Structural and mechanical characteristics of silk fibroin and chitosan blend scaffolds for tissue regeneration. *J Biomed Mater Res A* 2005;74:465-473.
- Pohl HA. Dielectrophoresis: The Behavior of Neutral Matter in Nonuniform Electric Fields. Cambridge, England: Cambridge University Press. 1979. p 1-579.
- Wang XJ, Wang XB, Gascoyne PRC. General expression for dielectrophoretic force and electrorotational torque derived using the Maxwell stress tensor method. *J Electrostat* 1997;39:277-295.
- Jones TB, Washizu M. Multipolar dielectrophoretic and electrorotation theory. *J Electrostat* 1996;37:121-134.
- Clague DS, Wheeler EK. Dielectrophoretic manipulation of macromolecules: the electric field. *Phys Rev E Stat Nonlin Soft Matter Phys* 2001;64(2 Part 2):026605.
- Arnold WM, Schwan HP, Zimmermann U. Surface conductance and other properties of latex particles measured by electroporation. *J Phys Chem* 1987;91:5093-5098.
- Bai X, Ma J, Pan Z, Song YH, Freyberg S, Yan Y, Vykoukal D, Alt E. Electrophysiological properties of human adipose tissue-derived stem cells. *Am J Physiol Cell Physiol* 2007;293:C1539-C1550.
- Altman AM, Matthias N, Yan Y, Song YH, Bai X, Chiu ES, Slakey DP, Alt EU. Dermal matrix as a carrier for in vivo delivery of

AQ2

AQ3

AQ4

- human adipose-derived stem cells. *Biomaterials* 2008;29: 1431–1442.
22. Zhang XY, La Russa VF, Reiser J. Transduction of bone-marrow-derived mesenchymal stem cells by using lentivirus vectors pseudotyped with modified RD114 envelope glycoproteins. *J Virol* 2004;78:1219–1229.
23. Lauffenburger DA, Linderman JJ. *Receptors: Models for Binding, Trafficking, and Signaling*. New York: Oxford University Press; 1993. 365 p.
- AQ5 24. Palsson B, Bhatia SN. *Tissue Engineering*. Pearson Prentice Hall; 2003. 407 p.
25. Palecek SP, Loftus JC, Ginsberg MH, Lauffenburger DA, Horwitz AF. Integrin-ligand binding properties govern cell migration speed through cell-substratum adhesiveness. *Nature* 1997;385: 537–540.
26. Bondar B, Fuchs S, Motta A, Migliaresi C, Kirkpatrick CJ. Functionality of endothelial cells on silk fibroin nets: Comparative study of micro- and nanometric fibre size. *Biomaterials* 2008;29: 561–572.
27. Stokes CL, Lauffenburger DA, Williams SK. Migration of individual microvessel endothelial cells: Stochastic model and parameter measurement. *J Cell Sci* 1991;99 (Part 2):419–430.



Author Proof

PROJECT 8

Development of Nanotherapeutics to Enhance Wound Healing

Joan Nichols, PhD (University of Texas Medical Branch)
Robert Advincula, PhD (University of Houston)

This project incurred spending during the third period of performance (September 2008 – September 2009) yet failed to complete an annual report. In March of 2009, Dr. Nichols communicated to our university that she was unable to complete the Year 2 report due to Hurricane Ike, which hit the Texas Gulf Coast in September 2008 and forced parts of UTMB to shut down for a period of several months. Through this communication, she stated her intent to complete the delinquent report as well as continue the research. Despite invoicing throughout the third performance period, Dr. Nichols again has failed to complete a report despite countless attempts to reach her.

PROJECT 9

Self-Assembling Peptide-Amphiphile Nanofiber Networks for the Controlled Growth and Differentiation of Dental Stem Cells

Jeffrey Hartgerink, PhD (Rice University)

Rena D-Souza, DDS, PhD (Texas A&M Health Science Center)

This project was completed at the end of the second performance period (September 2007 – September 2008) and did not report any spending beyond October 2008. Therefore, no annual report required for this project in the current performance period.

Alliance for NanoHealth Seed Grant

Title: Feasibility of selective laser elimination of leukemia cells targeted with gold and silver nanorods.

Final Progress Report February 3, 2010

Principal Investigator: Marina Konopleva, M.D., Ph.D.

Assistant Professor

Department of Blood and Marrow Transplantation

The University of Texas M.D. Anderson Cancer Center

1515 Holcombe Blvd., Unit 448

Houston, Texas 77030

Tel. 713-794-1628; Fax. 713-794-4747

Email: mkonople@mdanderson.org

Co-Investigator: Jason Hafner, Ph.D.

Associate Professor of Bioengineering,

Rice University

6100 Main Street

Houston, Texas 77005

Tel. 713-737 5870

Email: hafner@rice.edu

Co-Investigator: Alexander Oraevsky, Ph.D.

Vice President for Research and Development

Fairway Medical Technologies, Inc.

Houston, Texas 77099

Tel. 713-772-7867

Email: aoraevsky@fairwaymed.com

Background:

Despite recent advances in the chemotherapy of hematologic malignancies, a large proportion of patients remain incurable. ASCT is potentially curative treatment strategy, which is limited by the risk of re-infusion of residual tumor cells in the graft. While numerous purging methods have been developed, no existing method removes 100% of the tumor cells from the transplant. The nanotechnology of fabricating gold and silver nanorods has only recently become available. This project is based on the patented method of LANTCET, which uses gold NRs to enable selective *ex vivo* purging of tumor cells from a mixture with normal cells. Gold and silver nanorods (NR) possess very strong optical absorption tunable in the near-infrared spectral range (650 nm to 1100 nm) by changing their aspect ratio (of length to diameter). NPs can be targeted specifically to tumor cells using monoclonal antibodies (MAB). The cells loaded with gold NR can be detected using photothermal imaging and destroyed by laser-generated microbubbles (LMB) of vapor that emerge around the optically absorbing gold NRs. The proposed collaboration is aimed at developing an image-guided Laser Assisted NanoThermolysis Cell Elimination Technique (LANTCET) for purging of leukemia cells from autologous bone marrow or apheresis grafts.

AIMS:

1. Evaluate efficacy and safety of LANTCET technology with gold nanorods in model K562 cells based on protocols established earlier for spherical gold nanoparticles
2. Develop optimized protocol of conjugation, protocol of cell targeting, and protocol of laser treatment, methods for analysis of treated cells (dead and live).

Cells: Tumor model: K562, HL-60

MAB: CD33

Nanoparticles: Gold nanorods with aspect ratio of 3.6 (wavelength approximately 750-800 nm).

Laser: Pulsed laser 680-850 nm, energy of 100 mJ to create microbubbles around NR clusters

Methods

1. NR detection in individual cells: Flow Cytometry, Fluorescence Microscopy, SEM, Light Scattering Microscopy, silver stain
2. Cell damage detection: Concentration count (hemocytometer), Flow Cytometry Viability Count (live/dead fluorescence assay)

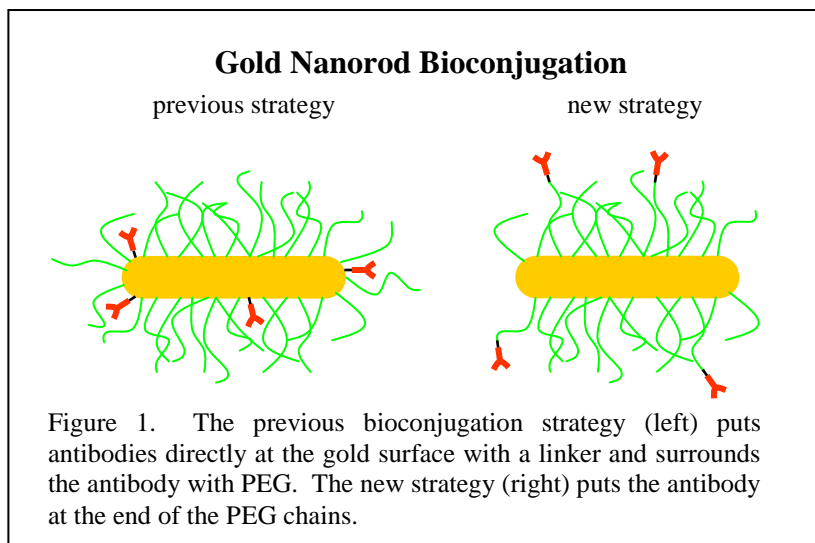
Summary of results:

1. Conjugation of nanorods to monoclonal antibody.

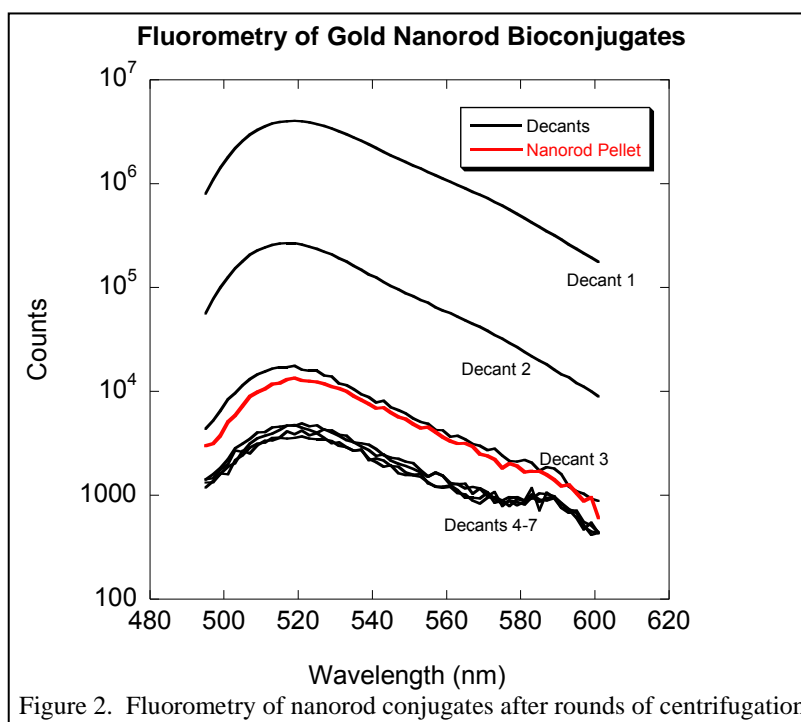
For successful application of gold nanorods to the LANTCET technology, the nanorods must be conjugated to monoclonal antibodies in such a way that the nanorods do not aggregate, antibodies remain attached to the nanorods, and the antibodies remain active.

Gold nanorods are synthesized in 0.1 M CTAB surfactant, and if this surfactant is removed, the rods will aggregate. Several strategies have been pursued to bioconjugated rods over the past year¹⁻⁴: electrostatic polymers, lipid conjugates, organic linkers, etc. Each of these has their difficulties and there is not yet a published method for targeting nanorods that has been repeated by a different group.

We started out with Hafner's method of PEGylating the nanorods and using an SPDP linker to attached antibodies to the nanorod surface.⁵ This was successful in strip plate assays, but several attempts with cells failed to show any sign of targeting. We believe the difference is that in the strip plate assays could incubate for 12 hours or more, while it is best to incubate with cells for a shorter time to show true targeting. This suggests that the antibodies were on the rod, but probably somewhat blocked by the PEG layer causing the need for long incubations. We therefore moved to a conjugation scheme where the antibody would be on the outside of the PEG layer by using a bifunctional PEG which exposes a carboxyl group at the free end. These COOH-PEG-NR were then coupled to antibodies by standard carbodiimide chemistry (NHS/EDC). This process does not aggregate the nanorods.



We have also developed simple analytical assays to test for successful conjugation. Although accumulation in cells gives the final proof, many problems can arise in such experiments that are not related to the bioconjugates. We conjugated anti-rabbit IgG labeled with Alexa Fluor 488 to gold nanorods as outlined above. During conjugation, the nanorods are at ca. 1 nM, and the AF488-IgG is at ca. 200 nM, so fluorometry of the resulting solution will be dominated by free AF488-IgG that is not bound to the nanorods. We therefore monitored the fluorometry as we took the conjugates through



several rounds of centrifugation, decant, and resuspension in buffer. By monitoring the fluorometry of the decants (which contain the free IgG) and the resuspended nanorod pellet (which contain both the remaining free and bound IgG), we can measure the conjugation yield. The fluorescence spectra in Figure 2 illustrate the method. Subsequent rounds of centrifugation produce decants with subsequently lower concentration of free AF488-IgG and therefore lower fluorescence, until the fluorescence signal reaches its noise floor. After all of the centrifugation steps, fluorometry of the resuspended pellet is measured, and it is found to be equivalent to the 3rd decant. This is fluorescence from the AF488-IgG bound to nanorods, and its concentration is also on the order of 1 nM, suggesting approximately 1 IgG per nanorod, which is reasonable considering their small size. This measurement is actually a lower limit since the fluorescence of the nanorod solution is reduced due to absorption of the nanorods.

The nanorod conjugation was also checked by electrokinetic analysis. The following table lists the zeta potential of CTAB stabilize nanorods, carboxylated PEG stabilized nanorods, and finally AF488-IgG conjugated nanorods.

	CTAB-NR	COOH-PEG-NR	IgG-PEG-NR
zeta potential	+85 ± 2 mV	-19 ± 2 mV	-5 ± 2 mV

The positive and negative values for cationic CTAB and anionic COOH-PEG were expected. Upon antibody conjugation, the zeta potential change to -5mV +/- 2 mV suggests a new molecule at the surface. The expected value is difficult to pin down since IgG pI's vary significantly and this experiment was carried out with polyclonal antibodies. However, the zeta potential analysis confirms that there has been a molecular change at the surface consistent with antibody conjugation.

2. Target nanorods to model K 562 and HL-60 cells, detect NR clusters in cells.

In the initial studies, we utilized commercial (Ted Pella) 20 nm streptavidin-conjugated nanospheres, either alone or conjugated to CD33 or to non-specific antibody C225. We examined different conditions of nanospheres targeting to leukemic cells HL-60 and K562. Different conditions included incubation of cells with NP at 4°, at 37°, or 4° incubation, wash, followed by incubation at 37°. The conditions were optimized to preserve good cell viability (>90%) following incubation with NP. The successful accumulation of NS in K562 cells was demonstrated by silver staining (Fig. 3).

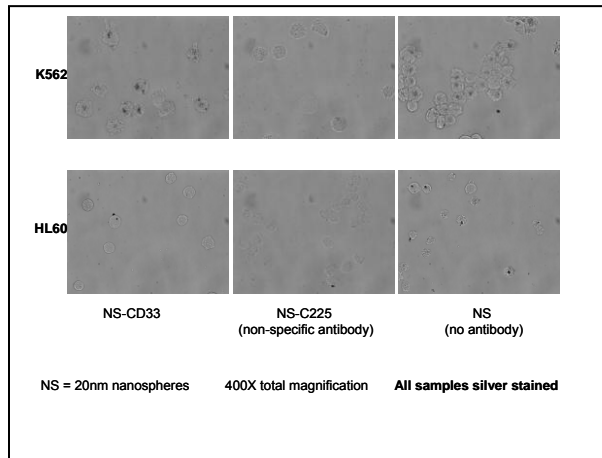


Figure 3. K562 or HL-60 were incubated with nanospheres alone, CD33-conjugated NS or C225-conjugated NS at 4°C for 30 minutes, then at 37°C for 30 minutes, followed by 2x washing in PBS. Cells were fixed and stained with silver stain. Nanospheres accumulation was evident in K562 but not in HL-60 cells.

2.2. In a separate experiment, K562 cells were incubated either with bare nanospheres alone or CD33-conjugated NS at 4°C for 30 minutes, then at 37°C for 30 minutes, followed by 2x washing in PBS. Cells were fixed and subjected to electron microscopy. Nanospheres accumulation was evident in K562 cells incubated with CD33-conjugated NS.

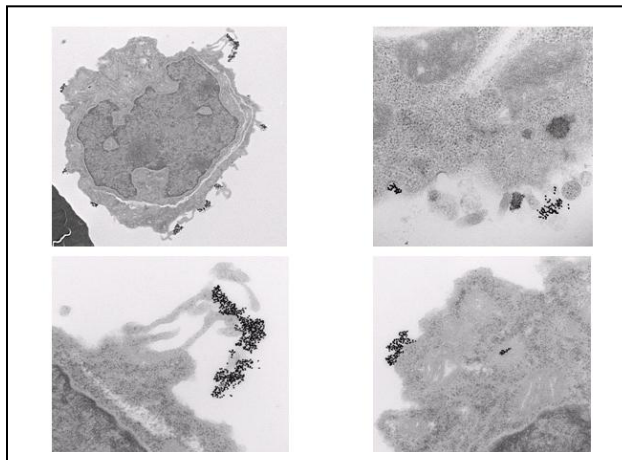


Figure 4. K562 cells were incubated with nanospheres alone (not shown) or CD33-conjugated NS at 4°C for 30 minutes, then at 37°C for 30 minutes, followed by 2x washing in PBS. Cells were fixed and subjected to electron microscopy. Nanospheres accumulation was evident in K562 exposed to CD33-conjugated NS but not in K562 cells exposed to bare NS (not shown).

2.3. We have developed new conjugation protocol for Ab-nanorods (Figure 5). The conjugates with anti-CD33 Ab have been made and have been tested in AML cell lines. The results demonstrate avid accumulation of CD33-conjugated nanorods in K562 cells (Figure 6).

Synthesis & Conjugation of Gold Nanorods

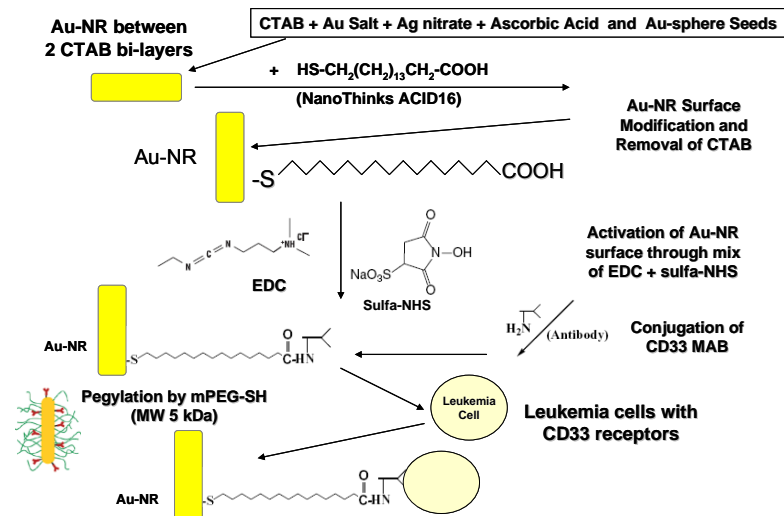


Figure 5. Schematic representation of conjugation CD33 Ab with gold nanorods.

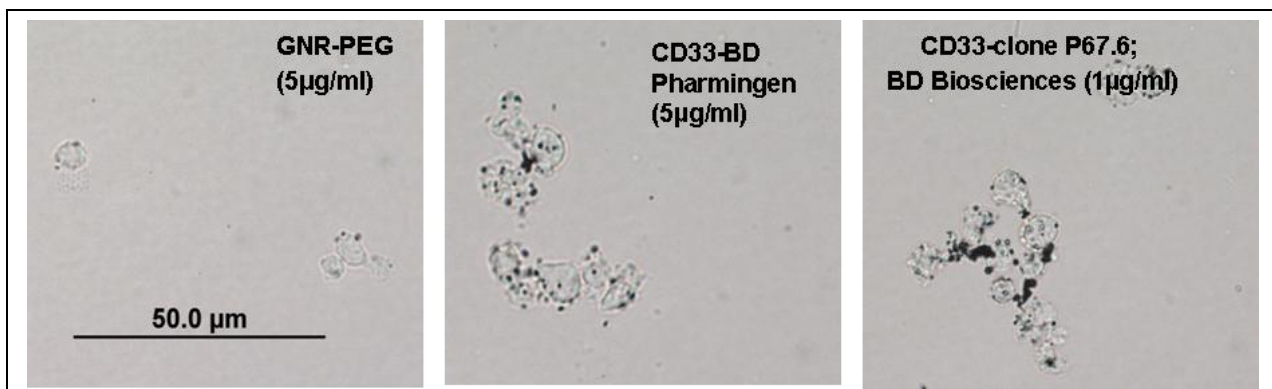


Figure 6. Silver stain of K562 cells after 1 hour pretreatment with conjugates: GNR-PEG (unconjugated); GNRods CD33 (BD Pharmingen); GNRods CD33 (BD Biosciences).